STUDY OF OPTICAL FIBER IN-LINE SENSORS BASED ON INNER AIR CAVITY

HU TIAN YI

M.Phil

The Hong Kong Polytechnic University

2014

The Hong Kong Polytechnic University

Department of Electrical Engineering

STUDY OF OPTICAL FIBER IN-LINE SENSORS BASED ON INNER AIR CAVITY

HU TIAN YI

A thesis submitted in partial fulfillment of the requirements for the degree of Master of Philosophy

March, 2014

CERTIFICATE OF ORIGINALITY

I hereby declare that this thesis is my own work and that, to the best of my knowledge and belief, it reproduces no material previously published or written, nor material that has been accepted for the award of any other degree or diploma, except where due acknowledgement has been made in the text.

(Signed)

HU Tianyi (Name of Student)

Abstract

Intrinsic fiber in-line sensors have attracted significant attention recently for their compact size, low cost and reliability. A number of methods to fabricate intrinsic fiber sensors have been reported. One of them is to fabricate fiber sensors based on inner air cavity.

By using femtosecond (fs) laser micromachining and fusion splicing technique, we could fabricate fiber inner air cavity and control the morphology of the cavity. Parameters controlling on fabrication process of the fiber in-line cavity have been investigated theoretically and experimentally. The size of the air cavity could be controlled from 30 μm to 93 μm during the fabrication process. In this thesis, four fiber sensors based on air cavity by using fs laser micromachining and fusion splicing technique would be proposed.

For a refractive index (RI) sensor use, we designed and fabricated an intrinsic Fabry-Perot interferometer (FPI) sensor based on inner air cavity. The interferometer cavity was formed by drilling a micro-hole at the cleaved fiber end facet, followed by fusion splicing. Two channels were drilled by fs to vertically cross the cavity to allow liquid to flow in and out. This device exhibits sensitivity of ~980 nm/RIU to ambient RI and low temperature cross sensitivity of ~4.8×10^{-6} RIU (refractive index unit) /°C.

We also developed a miniature fiber in-line Mach-Zehnder Interferometer (MZI) for high-temperature sensing at precise location. This MZI was based on an inner air cavity adjacent to the fiber core. After fabricating the air cavity adjacent to fiber core,

a microstructure was fabricated on the surface of the cavity by fs laser beam scanning to eliminate an unwanted set of interference fringe. Such a device is robust and insensitive to ambient RI change, and has high temperature sensitivity of ~43.2 pm/°C up to 1000°C, and low cross sensitivity to strain.

A platinum (Pt) -doped WO_3 composite coated fiber device based on fiber inner air cavity with periodical microstructures was proposed for hydrogen sensing. The fiber core was structural modulated by the microstructures, making this optical device sensitive to ambient RI change. Coated with Pt-doped WO3 composite, whose RI is changed through the variation of hydrogen concentration, this optical device became sensitive to hydrogen. Such a device is compact and exhibits a high sensitivity as well as a low temperature cross-sensitivity.

Based on dual internal mirrors formed by air spherical cavity surfaces, we also demonstrated another miniature fiber in-line cross-talk free MZI for simultaneous sensing for RI, temperature and curvature. We could monitor (1) RI by tracing output fringe visibility; (2) temperature by tracing fringe dip wavelength; (3) and curvature by tracing fringe dip intensity, respectively. No crosstalk between every two of these sensing results was found and no signal processing was required for this sensor. Such an inner structure-based fiber device is miniature, robust, suitable for high-accuracy measurement, sensitive to the surrounding environment, and free of temperature cross sensitivity, thus exhibiting high potential in versatile photonic applications.

Acknowledgement

First of all, I would like to express my sincere gratitude to my supervisor Dr. D. N. Wang for giving me the precious opportunity to do research in this fascinating area and for his invaluable supervision and encouragement throughout the whole period of my M.Phil period in the Hong Kong Polytechnic University.

I would like to thank Dr. Ying Wang, Dr. Changrui Liao, and Mr. Jun Ma for their guidance and help. Your technical support weights significantly on my way to peruse my degree. I own many thanks to my colleagues in Fiber Optics Laboratory for their kindly collaboration.

I want to express my gratitude to my family as well. You are my backup and you always encourage me to do the things I like.

Thank you all.

Contents

List of Figures and Tables

Chapter 1

Introduction

1.1 Background Review

In this chapter, review of fs laser technique and optical fiber sensors based on air cavity will be introduced. Development history of fs laser technique and features of fs laser micromachining will be demonstrated. After that, optical fiber sensors based on air cavity would be classified by fabrication methods, and several fiber sensors will be introduced.

1.1.1 Femtosecond Laser Technique

1.1.1.1 Development of Femtosecond Laser Technique

Since the invention of the ruby laser in 1960 [1], interaction between laser and different materials has drawn great attention all over the world. In order to obtain a suitable laser source for precise high quality micro machining, ultrashort duration pulse which allows high pulse repetition, high peak intensity and fast temporal resolution, has been proposed. The development of ultrashort pulses is shown in Fig. 1.1 [2].

In the early time of the research in ultrashort pulse, mode-locking technique has been proposed as a milestone [3]. In 1960s and 1970s, the mainstream of locking mode technique was operated by organic dye material, and its pulse duration is on

nanosecond scale. In 1981, by colliding pulse mode locking phase compensation, Fork generated ultrashort optical pulses in dye laser and the duration of laser pulse was compressed to less than 100fs for the first time [4]. The same group reported that by using cubic compensation technique, the pulse duration could be compressed to 6fs [5].

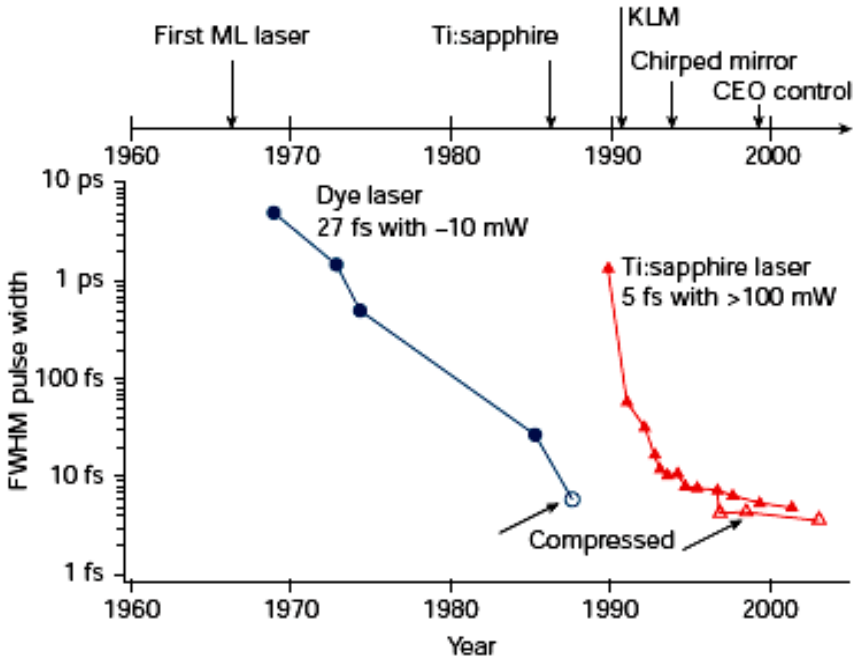

Fig. 1.1 Development of ultrashort optical pulses technique. [2]

In the late 1980s, solid-state laser crystals were developed and widely used for ultrashort pulse generation. Compared with dye laser, the size of solid-state laser is significantly reduced and the operation system is much simpler. Among the solid-state lasers, Ti:Sapphire (Ti:Al_2O_3) laser was considered to be one promising type of ultrashort pulse laser because of its broad gain bandwidth, wide emission bandwidth, high beam quality and reliability. A number of mode locking techniques have been developed [6-9].

In 1991, Haus in MIT revealed the mode locking mechanism of Ti:Sapphire laser-

Kerr lens mode locking, and compressed Ti: Sapphire laser pulse duration to several fs without external mode locking element [10,11]. To solve the intrinsic problem of the Ti:Sapphire that the mode locking condition is difficult to meet, semiconductor saturable absorber mirrors (SESAM) is applied to compressing system and enables the KLM easily self-start and work stably for a long time [12-14].

In 1985, chirped pulsed amplification (CPA) technique was developed by Strickland to meet the requirement of high peak power [15]. CPA is a technique for amplifying an ultrashort laser pulse up to the petawatt level by stretching out laser pulse temporally and spectrally prior to amplification. With rapid development of CPA, focused intensity has been increased since then [16-19].

1.1.1.2 Features of Femtosecond Laser Micromachining

Interactions between fs laser pulse and materials could be divided into two classes:

1) When pulse energy is below the damage threshold of the material, material refractive index is modulated by fs laser pulses [20-22]. This effect is often used in fabricating optical device. The mechanism of this effect is explained by a mix of theories like thermal effect, coloration, densification and fs laser introduced tension [23]. The value of the material RI changed is corresponding to single pulse energy, fs laser scanning speed, laser wavelength and pulse bandwidth [24].

2) When pulse energy is above the damage threshold of the material, irreversible damage would be made [25-27]. The degree of ablation on the material's surface counts on single pulse energy, amount of pulses within the fabrication process, pulse bandwidth and polarization of the laser.

Compared with long pulse laser, fs with ultrashort pulse duration and ultrahigh pulse peak power has great potential in the field of micromachining. In general, fs micromachining technique has three main advantages over CW or long pulse duration pulses [28]:

1. High accuracy. High accuracy attributes to two factors: less thermal effect and ultrasmall machining region. As multiphoton absorption is the leading effect in fs laser micromachining, the photon energy's deposition into materials could be performed in very short time, before the photon being transferred to surrounding lattice by means of phonon emission, which would introduce heat to the machining system. Therefore, there is little thermal influence by using femtosecond laser machining. Ultrashort pulse duration enables the interaction between fs laser and materials with little energy diffusion and ultrashort time duration. Within fabrication process, surrounding materials would not be melted by heat. Thermal diffusion and shockwave would be eliminated as well. Therefore, surface fabricated by fs laser micromachining would be much smoother compared with that machined by long pulse duration lasers [29].

   Fs laser could overcome the diffraction limit as well. Fs laser machining region would be controlled to less than the size of laser beam, whereas conventional laser machining technique accuracy is limited by the diffraction limit. Multiphoton absorption depends on the square (for two photo absorption) of the intensity distribution, and the value of the full-width at half-maximum (FWHM) of the intensity squared will be smaller than that of the intensity. Under this condition, the machining region is about the center of beam spot size and much smaller than the entire beam spot size [30].

2. Capability of three-dimensional fabrication in transparent materials. Transparent

materials like silica would not linearly absorb fs laser intensity, making it possible to fabricate structures inside these transparent materials by using fs laser micromachining technique [31].

3. Ability to be applied to any materials. Every material has a certain damage threshold energy based on multiphoton absorption mechanism. The threshold depends on the pulse energy. Therefore, with ultra-short duration and enough pulse energy, fs laser pulse could meet the threshold of almost all the materials and machine them, just like ceramics, silica, semiconductors and polymers [32].

1.1.2 Review of Optical Fiber Sensors Based on Air Cavity

Compared with electronic sensors, the optical fiber sensors have certain advantages that include immunity to electromagnetic interference, light weight, small size, high sensitivity, high flexibility, low propagating loss, low fabrication cost, simultaneous sensing ability, and ease in implementing multiplexed or distributed sensors [33]. Because of these advantages, the optical fiber sensors have attracted significant research attention [34]. A wide variety of fiber sensor types have been proposed, including fiber Bragg grating (FBG), long period grating (LPG), FPI, MZI, Michelson interferometer, distributed fiber sensor, and many others [34-40]. Almost every parameter, including temperature, RI, rotation, pressure, acoustic, strain, vibration, biologics, gases and humidity could be monitored by optical fiber sensors [34-40].

Among fiber sensors, fiber in-line intrinsic sensors have some advantages over extrinsic fiber sensors: (1) They are small in size and compact. (2) They are not

easily affected by environmental noise. (3) They have no extrinsic elements so their life expectancy is high. (4) They are immune to electronic interference [41].

However, to fabricate fiber in-line intrinsic fiber sensors like fiber in-line FPI is not an easy task. Laser irradiation is used for fabricating fiber in-line structures [42, 43]. However, structures fabricated by this technique exhibit rough surface and poor mechanical strength.

By combining these techniques with fusion splicing, fiber inner air cavity could be fabricated. Fiber inner air cavity by fusion splicing technique has smooth surface and hence reflected light may be coupled efficiently back into the guided mode rather than introduce optical loss because of scattering into cladding mode. Thus good visibility could be obtained. When the fusion current is relatively high and fusion time is relatively long, the fiber sensor with air cavity could be robust as well. There are three methods to fabricate an inner air cavity: (1) by using etching and fusion splicing technique (2) by partial collapsing technique and (3) by using fs laser micromachining and fusion splicing technique. We classify the fiber sensors based on air cavity according to fabrication technique and introduce them one by one.

1.1.2.1 Optical Fiber Sensor Based on Air Cavity by Using Etching and Fusion Splicing Technique

Etching technique is one method to fabricate fiber inner air cavity reported in 2006, by Xiaopei Chen for the first time [44]. Three steps are involved in the fabrication process: wet chemical etching, fusion splicing and cleave. Due the compositional difference between fiber core and fiber cladding, etching process on fiber core and on fiber cladding react at different rates. Core region would be etched more quickly by hydrofluoric acid than cladding region. After applying hydrofluoric acid to

cleaved fiber tip, a notch in the centre of the fiber tip would be found. Fig. 1.2 shows the differential etching process and result [44]. There is a clear semi-sphere notch in the centre of the fiber tip, and the fiber diameter is tapered from 128μm to 96μm. Splicing two etched fiber tips together by using an arc fusion splicer, an air cavity is fabricated. The notch is melted during the arc discharge process and expands into a smooth air cavity. Image of air cavity fabricated by using etching and fusion splicing technique is shown in Fig. 1.3. Sensors with two different structures: an intrinsic Fabry-Perot interferometer and a core-cladding-mode MZI are fabricated based on this structure.

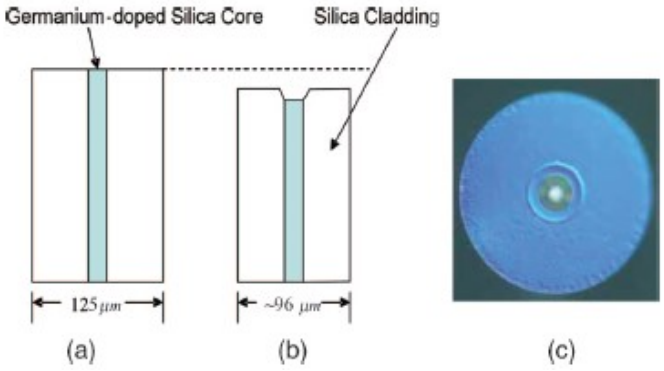

Fig.1.2 Differential wet chemical etching (a) before etching (b) after etching, (c) end face of the etched fiber. [44]

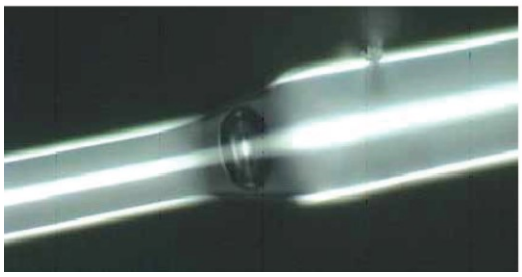

Fig.1.3 Image of air cavity fabricated by using etching and fusion splicing technique. [44]

In 2007, Machavaram proposed an alternative method to fabricated air cavity by using etching and fusion splicing technique [45]. Firstly, two cleaved single mode fiber tips are etched by hydrofluoric acid. Like the wet etching process in reference 44, there would be a notch at the centre of each fiber tip. Then these two etched fiber tips are fusion spliced with each other and an air cavity is fabricated. Fig. 1.4 shows

the fiber in-line FPI consisting of two semi-sphere notches. In this image, the air cavity is not a completed sphere or an ellipsoid. This is because the fusion current and fusion time are controlled at a small value. Air cavity is not totally melted during the arc discharge due to the lack of enough heat. An intrinsic FP interferometer is fabricated base on this air cavity.

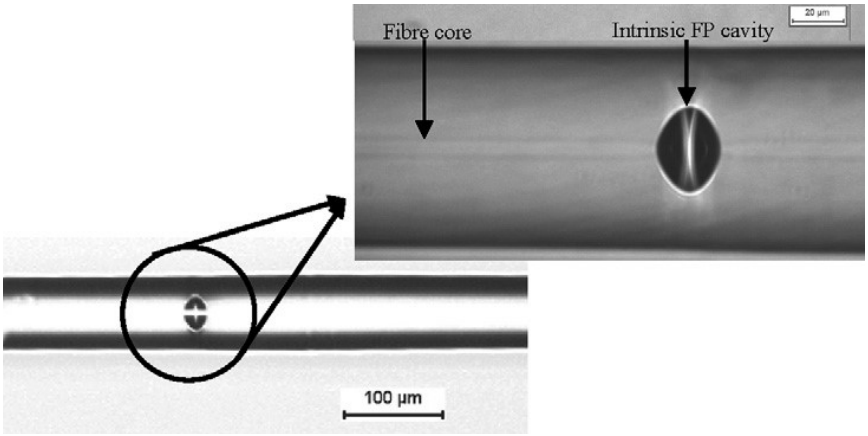

Fig 1.4 Image of air cavity by fusion splicing two notched fber tips. [45]

Machavaram also did the investigation into the mechanism of the reaction between silica and hydrofluoric acid. And the etching situations of cleaved fiber tip for 5 minutes, 12 minutes, 16 minutes, 22 minutes and 35 minutes have been investigated [45]. Fig. 1.5 shows the micro graph of cleaved fiber tip after different etching time from 0 minute to 35 minutes.

In the same year, a fiber in-line sensor for strain was proposed by Cibula based on air cavity. As shown in Fig. 1.6, one notch etched by hydrofluoric acid is carefully cleaved and spliced with two fiber tips to form a FPI sensor [46].

This technique provides a way to fabricate the fiber inner air cavity and could roughly control the morphology of the cavity. Nevertheless, fiber is tapered during the etching process. Fiber diameter decreases to less than 100 μm after the fabrication process, thus the mechanical strength of the sensor would be impaired.

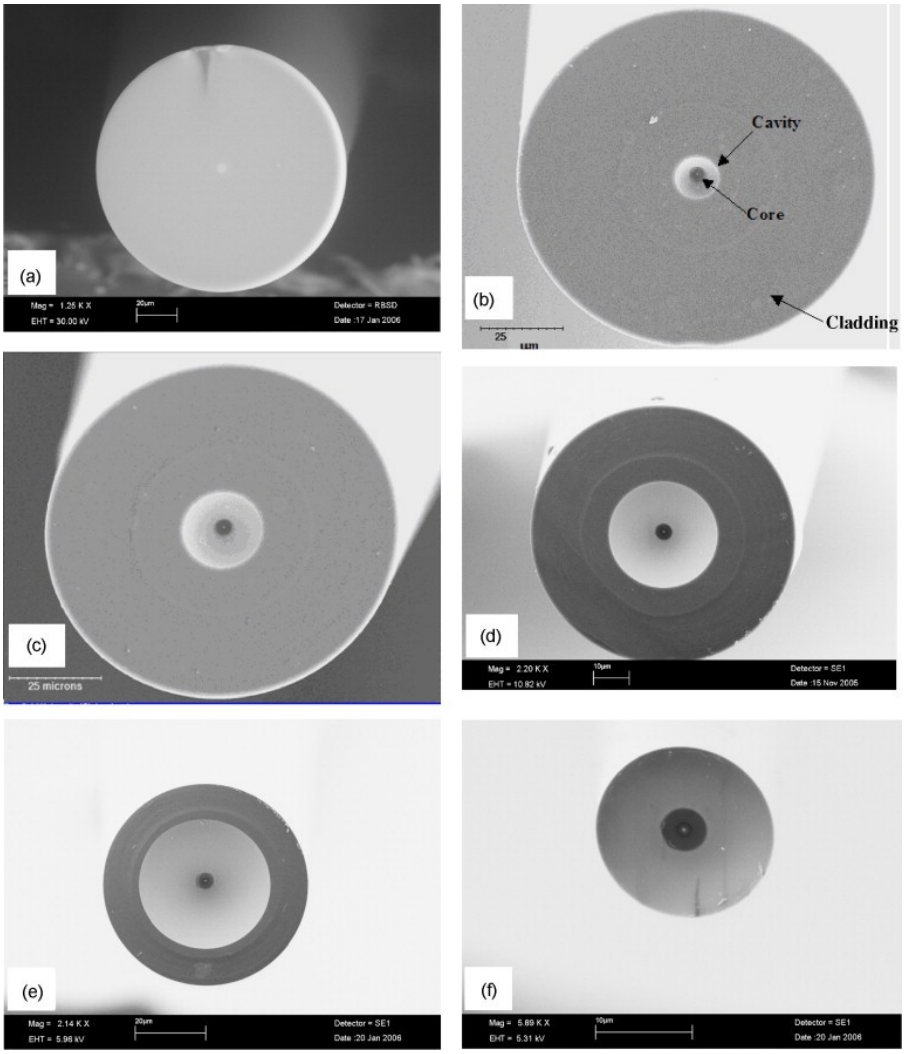

Fig. 1.5 Micro graph of cleaved fiber tip after etching for (a) 0 minute, (b) 5 minutes, (c) 12 minutes, (d) 16 minutes, (e) 22 minutes and (f) 35 minutes. [45]

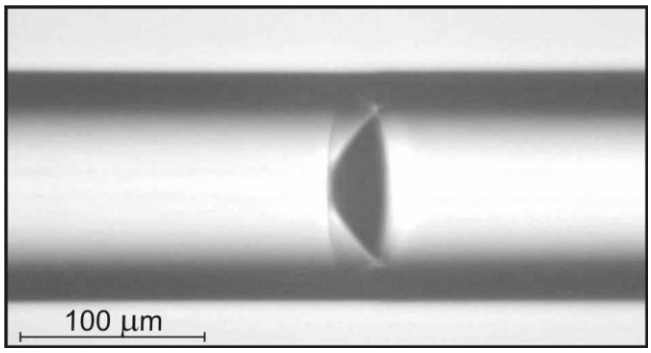

Fig.1.6 Image of air cavity fabricated by using etching and fusion splicing with fusion current of low value and short fusion time. [46]

1.1.2.2 Optical Fiber Sensor Based on Air Cavity by Partial Collapsing

There is another fabrication method based on splicing optical fiber with large fusion current to trap some air in the fiber to form air cavity. A number of special fibers have structure with air inside, such as PCF, capillary and hollow core fiber. When the fiber with air inside is spliced with large fusion current and long fusion time, the silica would be melted and air inside the fiber would expand to form an inner air cavity. Jun proposed a method to fabricate an air cavity for sensing in 2011. The air cavity is fabricated at the fiber tip by splicing a silica capillary to a single mode fiber and then melting the capillary to form a microsphere with an air cavity [47]. Fig. 1.7 shows the fabrication process.

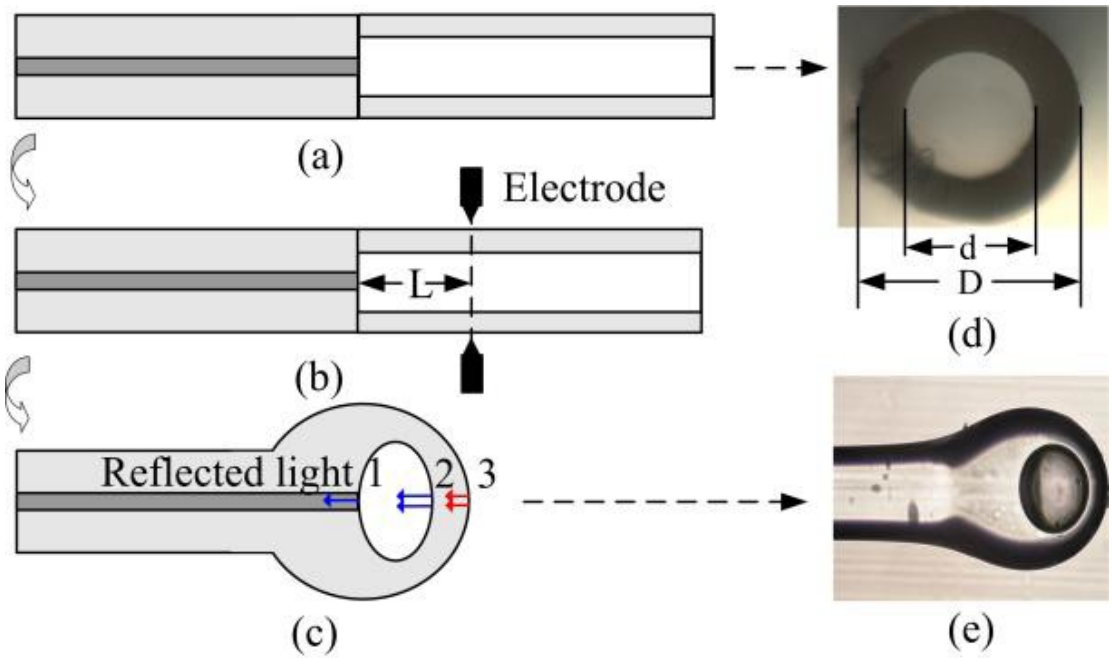

Fig. 1.7. Fabrication process of the air cavity. (a) Splice a silica capillary to a SMF; (b) heat and melt the capillary to form an air cavity (*L*: distance from electrode to the SMF end); (c) a sketch showing the fiber-tip micro-cavity; microscope image of (d) capillary cross-section and (e) micro-cavity. [47]

Partial collapsing PCF is also an alternative approach to fabricate an air cavity inside the fiber. By adjusting the fusion current to a large value, the air channels in PCF collapse, then part of air originally in the channels would be trapped, and after that an inner air cavity is formed due to surface tension [48]. In 2009, Villatoro reported a sensor for temperature and strain, with an inner air cavity fabricated by splicing a PCF to a SMF with a default fusion splicing program set for monomode fiber [49]. By adjusting the fusion splicing program, the diameter of the air cavity could be controlled from 22μm to 58μm [49]. In 2013, an intrinsic FPI was fabricated by similar method [50].

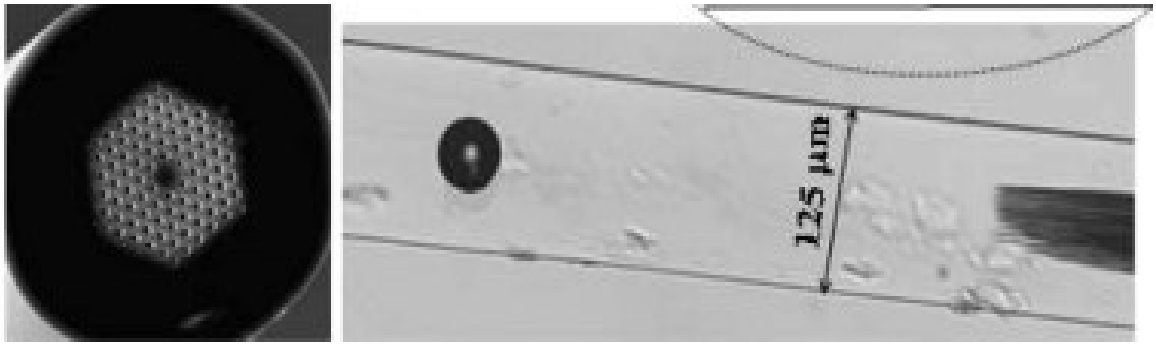

Fig.1.8 Image of the air cavity fabricated by collapsing the air channels in PCF. [49]

Recently, Duan reported a fiber FP sensor based on an inner air cavity formed by fusion splicing together two sections of SMFs with cleaved flat tip and arc fusion induced hemispherical tip, respectively [51]. Four steps are involved in this process: (1) Prepare two cleaved fiber tips. (2) Adjust the fusion splicing program to soften the cleaved fiber tip with prefusion cleaning discharge. A hemispherical is fabricated in this process. (3) Fusion splice the hemispherical tip with another cleaved fiber tip under a little external axes stress, and a slightly taper fiber with an air cavity is fabricated. (4) Several refusion discharges would be applied to the fiber to eliminate taper shape shown in Fig. 1.9 (c) [51].

Because no structural damage is in involved partial collapsing, robust fiber sensors based on inner air cavity could be fabricated this technique. However, the fusion splicing program is the only module could be adjusted; therefore we could not precisely control the morphology of the inner air cavity.

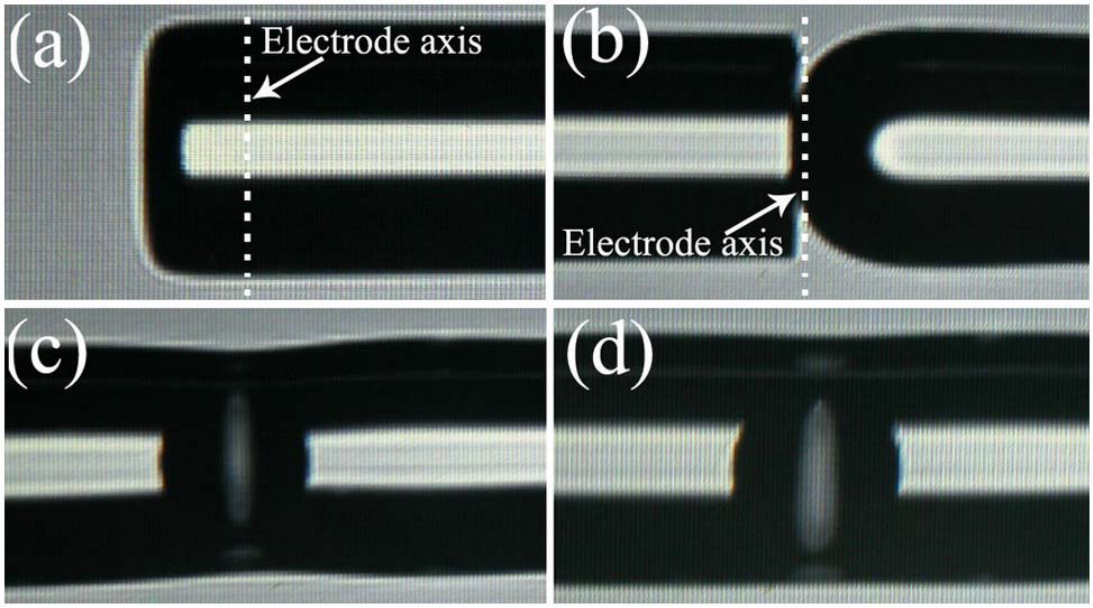

Fig. 1.9. Illustration of the fabrication procedure of air cavity based FPI strain sensor. [51]

1.1.2.3 Fiber Sensor Based on Air Cavity by Laser Micro-machining and Fusion Splicing

In 2008, Ran reported a FPI base on an air cavity fabricated by using laser micromachining for RI sensing [52]. They used a 157-nm laser to ablate a micro hole with diameter of 56μm at the centre of a fiber tip end, followed by splicing this fiber tip with another cleaved fiber tip to form a close air cavity. Microscopic image of the micro-hole and the sensor are shown in Fig. 1.10.

In 2009, Park proposed a fiber in-line MZI base on fiber inner air cavity. The MZI has optical path difference provided by a micro cavity of length ~10μm along a single mode fiber [53]. The fs laser focuses on the fiber tip cross section facet, after that a micro hole is ablated. After circularly irradiating, a cone shape micro hole is fabricated, as shown in Fig. 1.11. By controlling the size of the cone shape micro hole, the air cavity dimension after fusion splicing could also be adjusted.

Fs laser micromachining technique is a promising technique to fabricate the inner air cavity. Fiber sensors fabricated by using fs laser micromachining and fusion splicing are not tapered, exhibiting great mechanical strength. The morphology of ablated microhole and the fusion splicing program could be precisely adjusted during the fabrication process. Therefore we could control the morphology of the air cavity efficiently. And in this dissertation, we will use fs laser micromachining technique with fusion splicing to fabricate novel fiber sensors based on air cavities.

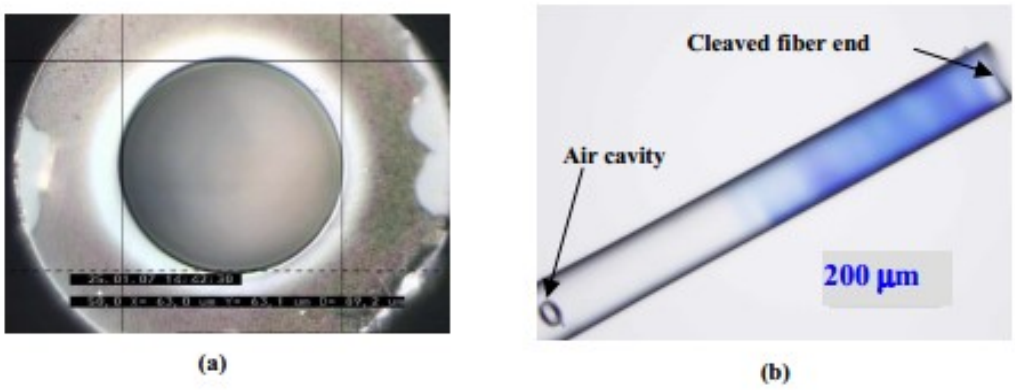

Fig.1.10. (a) Microscopic image of the micromachined hole introduced on the fiber cross section. (b) Microscopic image of the fabricated sensor head based on an air cavity. [52]

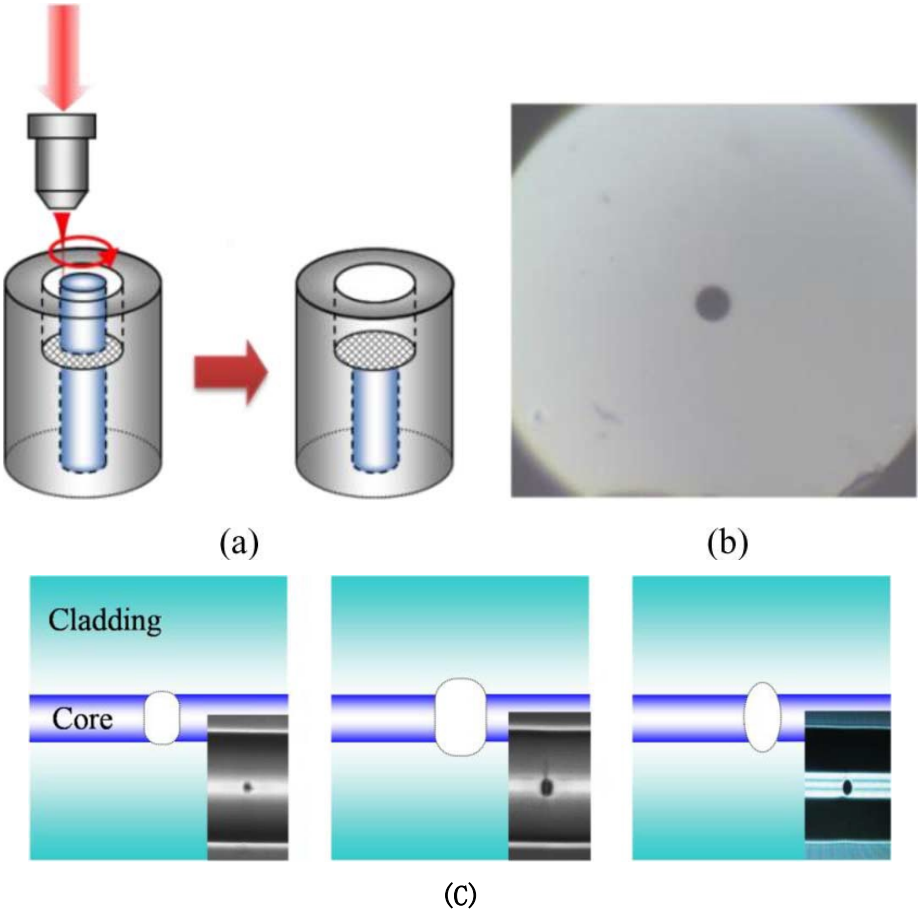

Fig.1.11 Fiber-inline MZI based on inner air cavity fabricated by fs laser (a) schematic fabrication process (b) cross section view (c) different cavity dimensions. [53]

1.2 Research Motivation and Contributions

Air cavity is one promising structure for intrinsic fiber in-line sensors. As mentioned in Section 1.1.2, a number of fiber sensors have already been proposed based on this structure. These sensors could be divided into two main types: intrinsic FPIs and core-cladding-mode MZIs. These two types of sensor are based on the air cavity at the centre of the fiber tip without any complementary microstructure. Unique and various advantages of fs laser micromachining technique like high accuracy and little thermal effect, make it a powerful tool to fabricate inner air cavity and control its morphology. We could also fabricate various types of microstructures on the surface

of the cavities with fs laser's capability of three dimensional fabrications in silica.

In this dissertation, based on air cavity, we are focusing on developing fiber sensors with high sensitivity, compact size, low cost, robust structure and ability to perform simultaneous sensing. Four novel intrinsic fiber sensors have been developed during my M.Phil study period:

- For a RI sensor use, Fabry-Perot cavity has been presented. The size of the cavity could be controlled by adjusting microhole diameter, fusion current and fusion duration. Two channels are drilled by fs to vertically cross the cavity to allow surrounding liquid to flow in and out. This device exhibits high sensitivity to ambient RI and low temperature cross sensitivity.

- A miniature fiber in-line MZI based on an inner air cavity adjacent to the fiber core for high-temperature sensing at precise location is demonstrated. When fiber core is abruptly bent and slightly damaged by the air cavity adjacent to fiber core, part of the light beam transmitting in the core would be coupled into to air cavity as leaky mode and then recombines with the core fiber mode at the end of the cavity. Howerver, the reflection effect introduced by air cavity smooth surface would decrease the coupling efficiency and lead to another unwanted interference. A microstructure is fabricated by fs laser scanning technique on the surface of the air cavity to make the surface rough and suppress the reflection effect. With that microstructure, unwanted interference fringe is eliminated and the visibility of the core-air cavity-mode MZ interference fringe is enhanced.

  Because the difference between the thermal temperature coefficient of fiber core and of air is much larger than that between fiber core and cladding, this device

exhibits high temperature sensitivity up to 1000°C, much higher than that of conventional core-cladding mode MZI temperature sensors. Thanks to the closed air cavity structure, such a device is also robust and insensitive to ambient RI change and has low cross sensitivity to strain.

- A Pt-doped WO_3 composite coated fiber device based on fiber inner air-cavity with periodical microstructures is proposed and demonstrated for hydrogen sensing in the thesis. An inner air-cavity adjacent to the fiber core exhibits periodic microstructures on the cavity surface and hence introducing a structure modulation on the fiber core, which converts part of the incident light beam into cladding mode, while the rest remain travels along the fiber core and as a result, loss dips appear in the transmission spectrum. The periodic microstructural device is similar to the micro-hole structured long period fiber grating and is sensitive to surrounding RI, but has a much smaller size.

  Pt-doped WO_3 is a metal compound that undergoes an exothermic reaction with hydrogen, and its RI increases during the reaction process. After coating Pt-doped WO_3 on fiber sensor based on air cavity with periodical microstructures, this device serves as a compact hydrogen sensor. Such a device is compact and exhibits high sensitivity as well as a low temperature cross-sensitivity.

- We also demonstrate a miniature fiber in-line MZI based on dual internal mirrors for simultaneous sensing. When the air cavity isadjacent to the fiber core, the smooth surface serves as an inner mirror reflecting the light beam in the fiber core to cladding. Thus a micro reflective optical path is built by two air cavity in the fiber. A compact device size is obtained corresponds to a large OPD and

hence a small FSR. A novel mechanism of interference is introduced by this structure.

For this sensor, change in ambient RI leads to a change in output fringe visibility, the variation in temperature only shifts the fringe dip wavelength, and the change in curvature merely causes a change in fringe dip intensity, i.e., three parameter sensing can be simultaneously achieved, and thus the temperature cross sensitivity can be eliminated.

1.3 Thesis Outline

Chapter 1 The fundamentals of fs laser micromachining technique and fiber sensors based on air cavity are reviewed in Section 1.1. Research motivation and contributions are illustrated in Secition 1.2.

Chapter 2 The principle of optical fiber FPI based on air cavity fabricated by fs laser micromachining and fusion splicing is investigated in Section 2.1. The fabrication of this optical device is introduced in Section 2.2. In Section 2.3 and 2.4, RI response and thermal response are investigated experimentally. Finally, a summary of Chapter 2 is presented in Section 2.5.

Chapter 3 In Section 3.1, principle of the fiber in-line MZI based on inner air cavity for high temperature sensing is investigated. In Section 3.2 fabrication process is introduced. High temperature response, RI response and axial strain response are investigated experimentally in Section 3.3, Section 3.4 and Section 3.5. Finally, a summary of Chapter 3 is presented in Section 3.6.

Chapter 4 Operation principle of a hydrogen sensor based on fiber inner air-cavity with microstructures is illustrated in Section 4.1. The fabrication process, including the inner air cavity, the microstructures and coating described in Section 4.2. Hydrogen response and thermal response are investigated in Section 4.3 and Section

4.4. Finally, a summary of Chapter 4 is presented in Section 4.5.

Chapter 5 In section 5.1 the principle of MZI based on dual inter mirrors formed by a hollow sphere pair is introduced. The fabrication process is demonstrated in Section 5.2. The influence of sphere pair length to the spectrum is tested Section 5.3. In Section 5.4, Section 5.5 and Section 5.6, strain response, thermal response and curvature response are investigated experimentally. In Section 5.7, we analyzed the polarization influence on this sensor. Finally, a summary of Chapter 5 is presented in Section 5.8.

Chapter 6 In the last chapter, the research contributions accomplished in this dissertation are summarized. Some potential improvements are discussed.

1.4 Publications

Journal Papers

1. **TY Hu**, DN Wang," Optical fiber in-line Mach–Zehnder interferometer based on dual internal mirrors formed by a hollow sphere pair" Optics Letters 38 (16), 3036-3039 (2013)
2. **TY Hu**, Y Wang, CR Liao, DN Wang, "Miniaturized fiber in-line Mach–Zehnder interferometer based on inner air cavity for high-temperature sensing" Optics Letters 37 (24), 5082-5084 (2012)
3. **TY Hu**, D. N. Wang, Minghong Yang, Min Wang, Jixiang Dai, "Miniature Hydrogen Sensor Based on Fiber Inner Cavity with Microstructures and Pt-doped WO3 coating", accepted by IEEE Photonics Technology Letters (2014)
4. X He, Z Liu, DN Wang, M Yang, **TY Hu**, JG Tian," Saturable absorber based on graphene-covered-microfiber" IEEE Photonics Technology Letters, 25 (14), 1392-1394 (2013)
5. CR Liao, **TY Hu**, DN Wang," Optical fiber Fabry-Perot interferometer cavity fabricated by femtosecond laser micromachining and fusion splicing for refractive index sensing" Optics Express 20 (20), 2813-22818 (2012)
6. Y Wang, DN Wang, CR Liao, **TY Hu**, J Guo, H Wei," Temperature-insensitive refractive index sensing by use of micro Fabry–Pérot cavity based on simplified hollow-core photonic crystal fiber", Optics Letters 38 (3), 269-271 (2012)
7. Y Wang, DN Wang, C Wang, **TY Hu**," Compressible fiber optic micro-Fabry-Pérot cavity with ultra-high pressure sensitivity" Optics Express 21 (12), 14084-14089 (2012)

8. X He, Z Liu, DN Wang (**TY H** being thanked)" Wavelength-tunable, passively mode-locked fiber laser based on graphene and chirped fiber Bragg grating" Optics Letters 37 (12), 2394-2396 (2012)

Conference Papers

1. **TY Hu**, DN.Wang, Ying Wang, and Changrui Liao "Inner air-cavity based fiber in-line Mach–Zehnder interferometer fabricated by femtosecond laser and fusion splicing (8924-193)", Oral Report on Asia Pacific Optical Sensors 2013 (APOS 2013), Wuhan, 15 Oct, 2013
2. **TY Hu**, DN Wang, "Optical fiber in-line Mach-Zehnder interferometer based on dual internal mirrors formed by a hollow sphere pair", Poster on Microoptics Conference 2013 (MOC 2013), Tokyo, 21 Oct, 2013

Reference

[1] T.Maiman, “Simulaterd optical radiation in ruby,” Nature, 187, 493-494 (1960)

[2] U. Keller, “Recent developments in compact ultrafast lasers,” Nature 424, 831-838 (2003)

[3] T. Dustech, “Mode-locking effects in an internally modulated ruby laser,” Appl. Phys. Lett. 7, 80-82 (1965)

[4] R. L. Fork, B. I. Greene, C. V. Shank, “Generation of optical pulses shorter than 0.1 psec by colliding pulse mode locking,” Appl. Phys. Lett., 38, 671-672 (1981)

[5] R. L. Fork, C. Cruz, P. C. Becker etal, “Compression of optical pulses to six femtoseconds by using cubic phase compensation,” Opt. Lett., 12, 483~485 (1987)

[6] R. Roy, P. A. Schulz, A. Walther, “Acousto-optic modulator as an electronically selectable unidirectional device in a ring laser,” Opt. Lett., 12, 672~674 (1987)

[7] N. Sarukura, Y. Ishida, H. Nakano et al. “CW passive mode locking of a Ti:sapphire laser,” Appl. Phys. Lett., 56, 814-815 (1990)

[8] P. M. W. French, S. M. J. Kelly, J. R. Taylor, “Mode locking of a continuous-wave titanium-doped sapphire laser using a linear external cavity,” Opt. Lett., 15, 378-380 (1990)

[9] K. Naganuma, K. Mogi, “50-fs pulse generation directly fron a colliding-pulse mode-locked Ti:sapphire laser using an antiresonant ring mirror,” Opt. Lett., 16, 738-740 (1991)

[10] D. E. Spence, P. N. Kean, W. Sibbett, “60-fsec pulse generation from a self-mode-locked Ti:sapphire laser,” Opt. Lett., 16, 42-44 (1991)

[11] H. A. Haus, J. g. Fujimoto, E. P. Ippen, “Structures for additive pulse mode

locking," J. Opt. Soc. Am. B, 8, 2068-2076 (1991)

[12] I. D. Jung, F. X. Kärtner, N. Matuschek et al. "Self-starting 6.5-fs pulses from a Ti:saphhire laser," Opt. Lett., 22, 1009-1011 (1997)

[13] D. H. Sutter, G. Steinmeyer, L. Gallmann et al. "Semiconductor saturable-absorber mirror-assisted Kerr-lens mode-locked Ti:sapphire laser producing pulses in the two-cycle regime," Opt. Lett., 24, 631-633 (1999)

[14] V. L. Kalashnikov, D. O. Krimer, I. G. Poloyko, "Soliton generation and picosecond collapse in solid-state lasers with semiconductor saturable absorbers," J. Opt. Soc. Am. B, 17,519-523 (2000)

[15] D. Strickland, G. Mourou, "Compression of amplified chirped optical pulses," Opt. Commun., 56,219-221 (1985)

[16] A. Sullivan, H. Hamster, H. C. Kapteyn et al, "Multiterawatt, 100-fs laser," Opt. Lett., 16,1406-1408 (1991)

[17] V. V. Lozhkarev, K. Yamakawa, Y. Akahane et al, "0.85-PW, 33-fs Ti:sapphire laser," Opt. Lett., 28, 1594-1596 (2003)

[18] M. Martinez, E. Gaul, T. Ditmire et al, "The Texas Petawatt Laser," Proc. Of SPIE, 5991: 59911N (2005)

[19] T. Tajima, G. Mourou, "Zettawatt-exawatt lasers and their applications in ultrastrong-field physics," Phys. Rev. Special Topics-Accelerators and Beams, 5, 031301 (2002)

[20] C. Schaffer, A. Brodeur, J.Inouye et al, "Micromachining bulk glass by sue of femtosecond laser pulses with nanojoule energy," Opt. Lett., 26, 93-95 (2001)

[21] K. Miura, J.Qiu, H.Inouye et al, "Photowritten optical waveguides in various galsses wit ultrashort pulses laser pulses," Opt. Lett., 24, 1311-1313 (1999)

[22] D.Homoelle, S. Wielandy, A. Gaeta et al, "Infrared photosensitivity in silica glasses exposed to femtosecond laser pulses," Opt. Lett., 24, 1311-1313 (1999)

[23] A. Streltsov, F.Borrelli, “Study of femtosecond-laser-written waveguides in glasses,” J. Opt. Soc. Am. B, 19, 2496-2504 (2002)

[24] H.Guo, H.Jiang, Y. Fang et al, “The pulse duration dependence of femtosecond laser induced refractive index modulation in fused silica,” J. Opt. A: Pure Appl. Opt., 6, 787-790 (2004)

[25] M. Lenzner, J. Kruger, S. Sartania et al, “Femtosecond optical breakdown in dielectrics,” Phys. Rev. :Lett., 80, 4076-4079 (1988)

[26] A. Joglekar, H.Liu, E.Meyhofer et al, “Optics at critical intensity: Applications to nanomorphing,” Proc. Nat. Acad. Sci. USA, 101(16), 5856-5861 (2004)

[27] B. Stuart, M. Feit, S. Herman et al, “Nanosecond-to-femtosecond laser-induced breakdown in dielectrics,” Phys. Rev. B, 53(4), 1749-1761 (1996)

[28] X. Liu, D. Du, G. Mourou, “Laser ablation and micromachining with ultrashort laser pulses,” IEEE J. Quantum Electron., 33, 1706-1716 (1997)

[29] B. N. Chichkov, C. Momma, S. Nolte, et al, “Femtosecond, picosecond and nanosecond laser ablation of solids,” Appl. Phys. A 63, 109-115 (1996)

[30] S. Jeon, V. Malyarchuk, J. A. Rogers, et al, “Fabricating three dimensional nanostructures using two photon lithography in a single exposure step,” Opt.Express 14, 2300-2308 (2006)

[31] S. Maruo, K. Ikuta, H. Korogi, “Submicron manipulation tools driven by light in a liquid,” Appl. Phys. Lett. 82, 133-135 (2003).

[32] M. D. Perry, B. C. Strart, P. S. Banks, et al, “Ultrafast-pulse laser machining of dielectric materials,” J. Appl. Phys. 85, 6803-6810 (1999)

[33] Byoungho Lee, “Review of the present status of optical fiber sensors, Optical Fiber Technology,” 9, 57-79 (2003)

[34] A. D. Kersey, “A review of recent developments in fiber optic sensor technology,” Optical Fiber Technology, 2, 291-317 (1996)

[35] B. Lee, “Review of the present status of optical fiber sensors,” Opt. Fiber Technology, 9, 57-79 (2003)

[36] K. T. V. Grattan, B. T. Meggitt, Optical Fiber Sensor Technology, Kluwer Academic publisher: Boston (1999)

[37] B. Culshaw, J. Dakin, Optical Fiber Sensors, Artech House: Boston (1988)

[38] F. T. S. Yu, S. Yin, Fiber Optic Sensors, Dekker: New York (2002)

[39] A. Othonos, K. Kalli, Fiber Brag Gratings-Fundamentals and Applications in Telecommunications and Sensing, Artech House: Boston (1999)

[40] T. G. Giallorenzi, J. A. Bucaro, A. Dandridge, et al, “Optical fiber sensor technology,” IEEE J. Quantum Electron. 18, 626-65 (1982)

[41] Peter M. Tracey, “Intrinsic Fiber-optic Sensors,” IEEE transaction on industry applications 27, (I) (1991)

[42] B. Stuart, M. Feit, S. Herman et al.. “Nanosecond-to-femtosecond laser-induced breakdown in dielectrics,” Phys. Rev. B, 53, 1749-1761 (1996)

[43] X. Liu, D. Du, G. Mourou, “Laser ablation and micromachining with ultrashort laser pulses,” IEEE J. Quantum Electron 33, 1706-1716 (1997)

[44] Xiaopei Chen, Fabin Shen, Zhuang Wang, Zhenyu Huang, and Anbo Wang; “Micro-air-gap based intrinsic Fabry–Perot interferometric fiber-optic sensor,” App. Opt., 45, 7760-7766 (2006)

[45] V.R. Machavaram, R.A. Badcock, G.F. Fernando, “Fabrication of intrinsic fibre Fabry–Perot sensors in silica fibres using hydrofluoric acid etching," Sensors and Actuators A 138, 248-260 (2007)

[46] Edvard Cibula, Denis Donlagic, “Review of Air cavity Structure in Fiber Sensing In-line short cavity Fabry-Perot strain sensor for quasi distributed measurement utilizing standard OTDR,” Opt. Express, 15, 8719-8730 (2007)

[47] Jun Ma, Jian Ju, Long Jin, et al “Fiber-tip micro-cavity for temperature and transverse load sensing,” Opt. Express 19, 12418-12426 (2011)

[48] Joo Hin Chong and M. K. Rao, "Development of a system for laser splicing photonic crystal fiber," Opt. Express, 11, 1365-1370 (2003)

[49] Joel Villatoro, Vittoria Finazzi, Gianluca Coviello, et al; “Photonic-crystal-fiber-enabled micro-Fabry–Perot interferometer,” Opt. Lett. 34, 2441-2443 (2009)

[50] Daniel Jáuregui-Vázquez, Julián M. et al “An All Fiber Intrinsic Fabry-Perot Interferometer based on an Air-Microcavity,” Sensors, 13, 6355-6364 (2013)

[51] De-Wen Duan, Yun-jiang Rao, Yu-Song Hou, et al, "Microbubble based fiber-optic Fabry–Perot interferometer formed by fusion splicing single-mode fibers for strain measurement," Appl. Opt. 51, 1033-1036 (2012)

[52] Z. L. Ran, Y. J. Rao, W. J. Liu, et al “Laser-micromachined Fabry-Perot optical fiber tip sensor for high-resolution temperature-independent measurement of refractive index,” Opt. Lett. 16, 2252-2263 (2007)

[53] Minkyu Park, Sejin Lee, Woosung Ha, et al “Ultracompact Intrinsic Micro Air-Cavity Fiber Mach–Zehnder Interferometer,” IEEE Photo. Tech. Lett. 21, 1027-1029 (2009)

Chapter 2

Optical Fiber Fabry-Perot Interferometer Cavity Fabricated by Femtosecond Laser Micromachining and Fusion Splicing for Refractive Index Sensing

Optical fiber FPI cavity has been attractive for many sensor applications owing to its miniature size, in-line structure, linear response, high sensitivity and convenient reflection mode of detection [1-10]. To enable effective RI sensing, the optical fiber FPI should be constructed into a tip device for flexible liquid immersion or built with an open micro-cavity to allow liquid to flow in. In such schemes, the conventional SMF needs to be incorporated with in-fiber mirrors [7], or spliced with a section of photonic crystal fiber [8, 9]. However, these fabrication methods are rather complicated or with relatively high cost. In recent years, near-IR fs laser has been widely used for fabricating photonic devices in transparent materials such as bulk glasses [11, 12] and different types of optical fibers [13-15]. Many micro-cavities have been fabricated in optical fiber by using fs laser micromachining and operated as fiber in-line interferometers, such as FPIs [3, 7, 10] and MZIs [16-18]. However, such fiber in-line interferometers, directly fabricated by fs laser ablation, usually exhibit rather rough cavity surface and poor mechanical strength.

In this chapter, a fiber in-line FPI cavity fabricated by using fs laser micromachining together with fusion splicing is presented for RI sensing. The FPI cavity is formed by drilling a micro-hole at the end facet of SMF, followed by fusion splicing, and

finally inscribing a micro-channel by fs laser micromachining to vertically cross the cavity and allow the RI liquid to flow in. Such a RI sensor is simple in structure, easy for fabrication and reliable in operation. The RI sensitivity obtained is ~994nm/RIU with low temperature cross-sensitivity of ~4.8 × 10^{-6} RIU/°C. The fabrication process, parameters controlling, RI response and thermal response of the FPI sensor have been investigated in this chapter.

2.1 Operation Principle of Fiber In-line FP Interferometer

Fig. 2.1 shows the schematic of the FPI sensor system proposed, in which a hollow sphere with vertical opening serves as the FP cavity. The incident light beam along the SMF is reflected by the two surfaces of the sphere respectively and recombined in the fiber core, resulting in an interference pattern at the output.

Assuming that the reflected light beam intensities by the two surfaces of the FP cavity are I_1 and I_2, respectively, the intensity of the interference signal is:

$$I = I_1 + I_2 + 2\sqrt{I_1 I_2}\cos(\frac{4\pi nL}{\lambda} + \varphi_0) \tag{2.1}$$

where λ is the wavelength of incident light, n is the RI of the liquid filled in the cavity, L is the cavity length and φ_0 is the initial phase of the interference. At the fringe dip positions, the phase difference of the two reflected light beams satisfies the condition

$$\frac{4\pi nL}{\lambda_m} + \varphi_0 = (2m+1)\pi \tag{2.2}$$

where m is an integer, λ_m is the central wavelength of m^{th} order interference dip. According to Eq. (2), the dip wavelength depends on the cavity length and the RI of

the liquid filled in the cavity. Meanwhile these two factors are also functions of temperature and the wavelength shift as the temperature is given by:

$$\frac{4\pi nL}{\lambda_m} + \varphi_0 = (2m+1)\pi \tag{2.3}$$

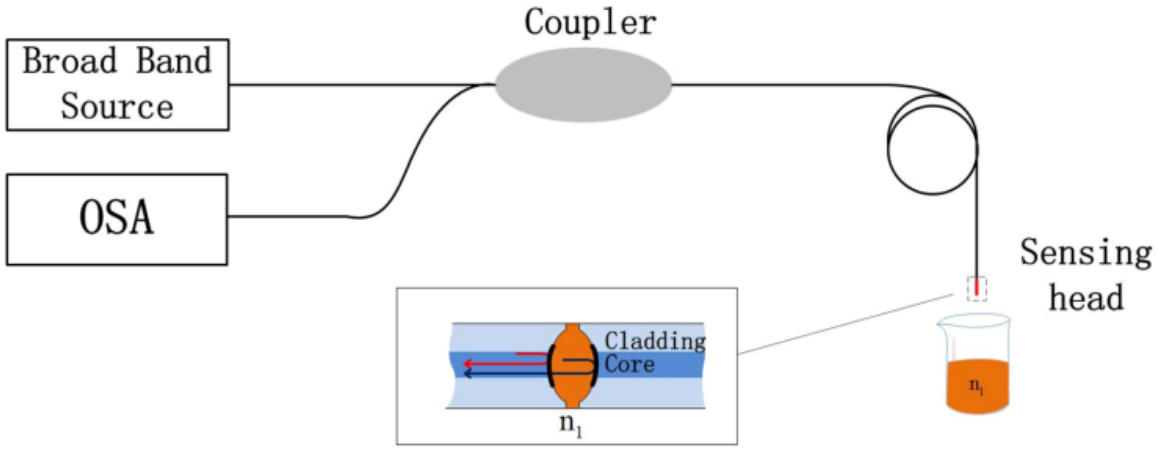

Fig. 2.1 Experimental setup for RI measurement.
The inset shows the schematic diagram of the fiber FPI.

2.2 Fabrication of Fiber In-line FP Interferometer

2.2.1 Device Fabrication

The experimental setup for RI measurement is shown in Fig. 2.1. The fs laser pulses (120fs, 1mJ, 1 kHz repetition rate at λ=800nm) are produced by a Ti: Sapphire CPA laser system (Spectra-Physics). The laser beam is focused onto the fiber in the device fabrication, fs laser pulses (λ = 800 nm) of 120 fs at the repetition rate of 1 kHz were focused onto the fiber end facet by a 20 × objective lens with NA value of 0.5 and working distance of 2.1mm. The pulse energy used in the experiment was ~2 μJ. A CCD camera was employed to monitor the fabrication process and record the sample morphology.

A section of standard SMF-28 with the core diameter of 8.2 μm and the nominal effective RI of 1.4682 (at 1550 nm) was mounted on a computer controlled three-dimensional translation stage with a 40-nm resolution. The following steps were adopted in the fabrication process as illustrated in Fig. 2.3. Firstly, fs laser drilled a micro-hole of ~1 μm in diameter at the centre of the cleaved fiber end facet, and the fiber tip obtained was then spliced together with another cleaved SMF tip without micro-hole by a fusion splicer (ERICSSON FSU975), with fusing current and fusing duration of 16.3 mA and 2.0 s respectively. The hollow sphere formed had a diameter of ~60 μm. Finally, a micro-channel of ~38 μm in diameter was machined to vertically cross the FP cavity, which allowed the RI liquid to readily flow in or out of the cavity. In the micro-channel fabrication process, laser beam was firstly focused on the top fiber surface at the micro-cavity position, scanned at a speed of 2 μm/s with a scanning distance of 40 μm, in parallel to the fiber core axis. After one scanning cycle, the laser beam was shifted by 10 μm, in perpendicular to the fiber axis until a 40μm × 40μm square area was drilled through, to create the top part of the micro-channel. The fiber was then rotated by 180° to allow fabrication of the bottom part of the micro-cavity, following the same procedure as mentioned above.

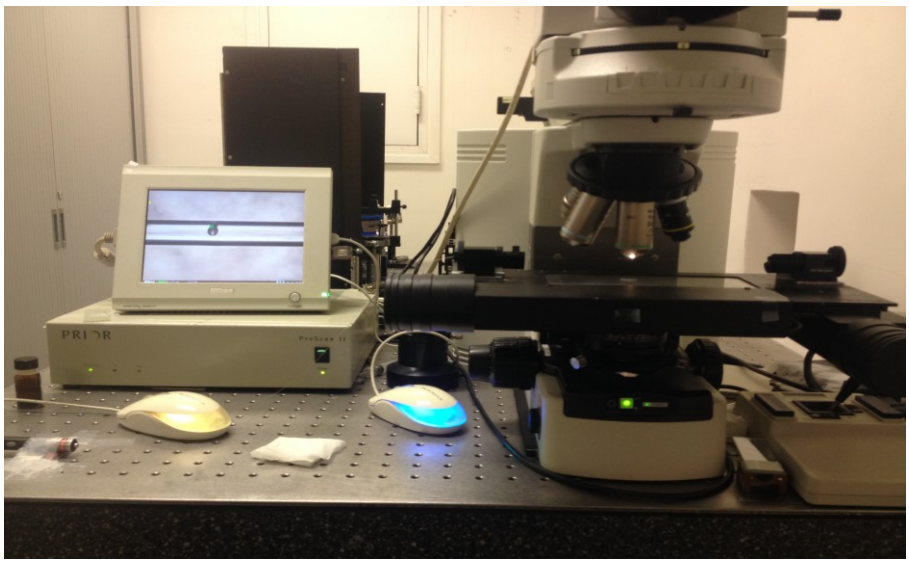

Fig. 2.2 Set up for the fabrication system.

It should be mentioned that the system actually has two FP cavities. The second FP cavity is formed by the hollow sphere surface and the fiber end immersed in the liquid. Since the reflected light beam from the hollow sphere surface is divergent, and a large curvature of the hollow sphere surface corresponds to a large reflection light divergence, the interference fringe pattern of the second FP cavity is critically dependent on the cavity length. When the cavity length is large, the reflected light beam intensity is very small, which leads to an extremely poor fringe visibility and as a result, the corresponding fringe pattern can hardly be observed. In our experiment, the second cavity length is ~40 mm and the fiber end immersed in the liquid is not cleaved, thus no corresponding fringe can be observed.

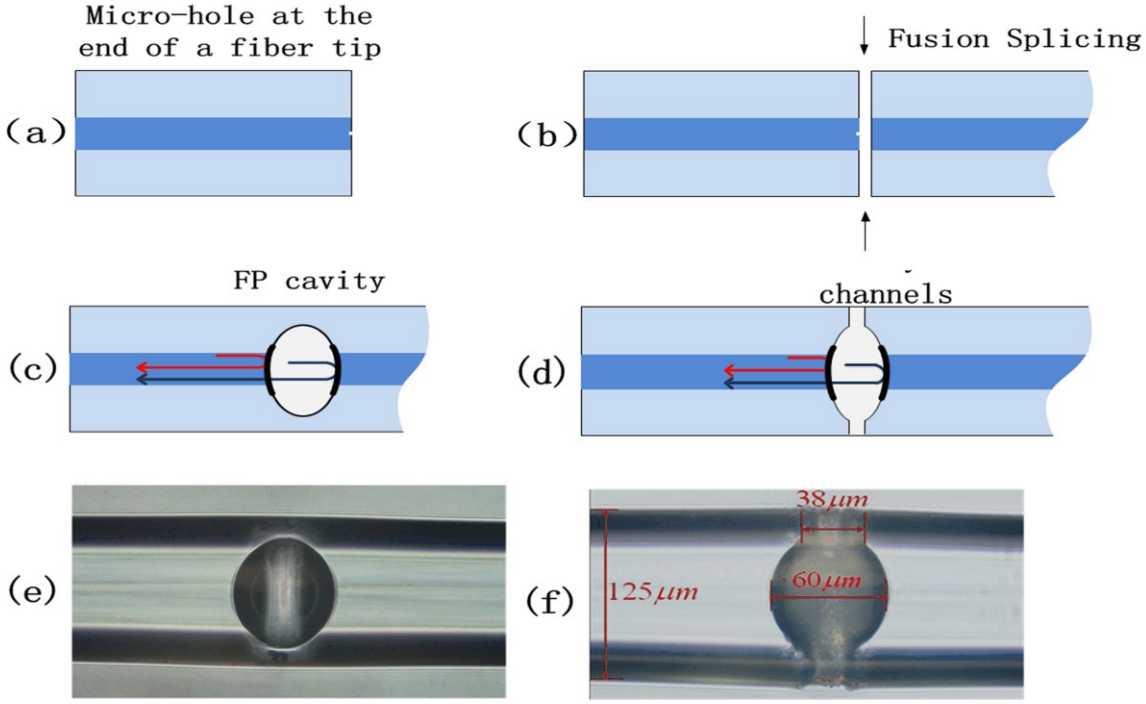

Fig. 2.3 Fabrication process of fiber in-line FPI. (a) The femtosecond laser creates a micro-hole of ~1 μm in diameter at the centre of cleaved fiber end facet. (b) The fiber tip with the micro-hole spliced together with another cleaved SMF tip. (c) FP cavity formed. (d) To fabricate a micro-channels to vertically cross the micro-cavity. (e) Microscope image of the fiber in-line FPI cavity without the micro-channel. (f) Microscope image of the fiber in-line FPI cavity with the micro-channel.

2.2.2 Fabrication Parameter Controlling

By changing the size of initial micro-hole and the fusion splicing parameters, the hollow sphere of different sizes and hence different cavity lengths can be created. Figure 2.4(a) shows three hollow spheres with different cavity lengths of 30, 65 and 93 μm respectively, corresponding to the initial micro-hole diameter of 1, 1 and 10 μm, the fusion current of 15.3, 16.8 and 17.3 mA, and the fusion duration of 1.5, 2.0, and 2.0 s, respectively. The reflection spectra corresponding to different cavity lengths are displayed in Fig. 2.3(b). It can be found from this figure that, with the increase of cavity length from 30 μm to 93 μm, the fringe spacing around 1550 nm is decreased from 39.3 nm to 12.9 nm. The fringe spacing variation around 1550 nm with the air-cavity length was calculated according to Eq. (2.3), and the results obtained are shown in Fig. 2.3(c), where the black line stands for the calculated results and the red squares represent the experimental values obtained in Fig. 2.3(b). The experimental results agree well with the simulations based on FPI theory.

Figure 2.4(b) shows that the reflection intensity monotonically goes up with the increase of cavity length. This is due to the fact that with a larger radius of the hollow sphere, the two reflection surfaces within the fiber core are nearly in parallel and hence the reflected light intensity can be enhanced. However, the fringe visibility does not change in a monotonic manner when the cavity length is increased as it depends also on surface reflectivity and propagation loss in the cavity.

The size of the vertical micro-channel should be properly chosen to facilitate the RI liquid flow in and out of the FPI cavity. The micro-channel size of 20 and 38 μm were tested in the experiment, and the time taken for the liquid to be fully filled in the cavity was 15 minutes and a few seconds, respectively. The dependence of the

filling time of the liquid on the size of micro-channel is due to the dependence of air pressure inside the micro-cavity on the size of micro-channel. When the sample is immersed into the liquid, the air pressure inside the micro-cavity would prevent the liquid to flow in. If the micro-channel size is small, the air would slowly escape from the cavity and thus the filling time of the liquid is long. When the channel size becomes large, the air can quickly escape from the micro-cavity and a short filling time of the liquid can be achieved. Since the micro-channel is located purely in the cladding area, its size has no essential effects on the interference spectrum. However, a large channel size would reduce the robustness of the device.

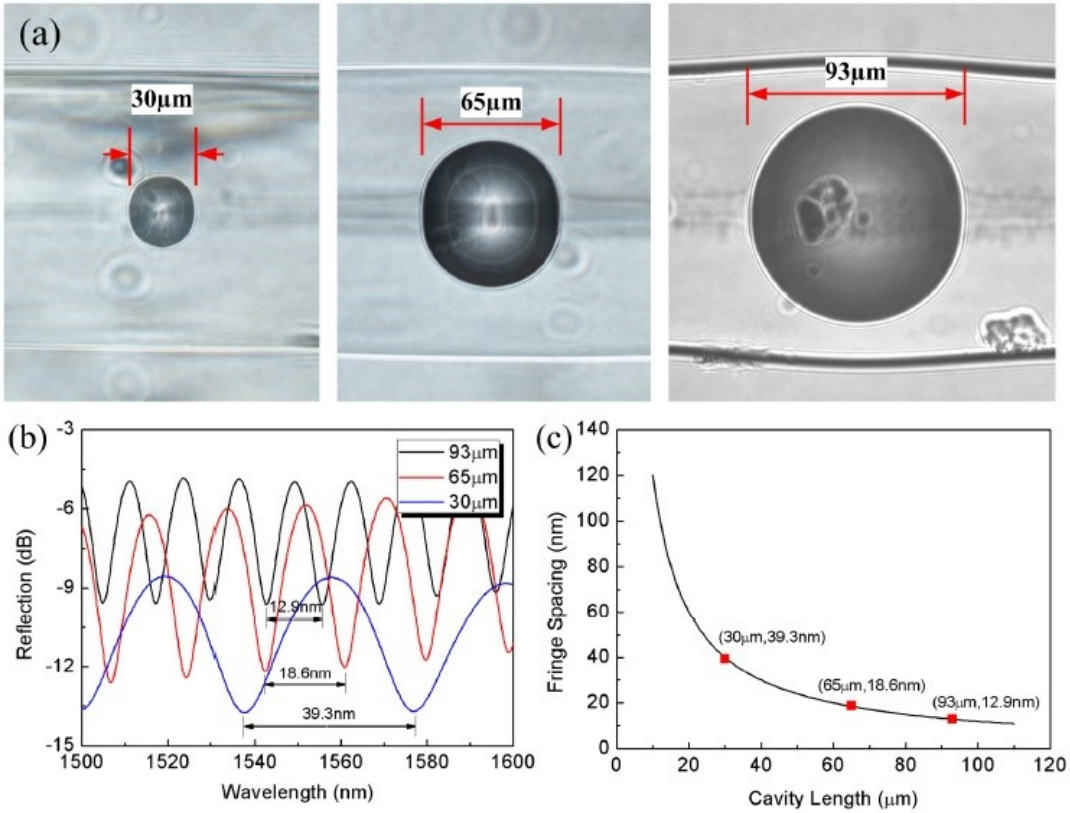

Fig.2.4 (a) Microscope images of the FPI cavity with length of 30, 65 and 93 um, respectively.(b) Reflection spectra of fiber in-line FPI with different cavity lengths. (c) Simulated fringe spacing as a function of cavity length at the wavelength of 1550 nm. The black line is the calculation result and the red square shows the experimentally obtained value.

2.1 Refractive Index Response

The RI measurement by the use of fiber in-line FP cavity was carried out at room temperature by immersing the sensor head in the RI liquids. Each time after the measurement, the device was rinsed with Propyl alcohol carefully until the original spectrum was restored and no residual liquid was left. The reflection spectra were monitored in real-time by use of an optical spectrum analyzer (OSA) with a resolution of 0.01 nm.

Figure 2.5(a) shows the reflection spectra corresponding to the RI values of 1.315, 1.32 and 1.325, respectively, and a red shift of dip wavelength can be clearly observed. The transmission dip wavelength corresponding to different RI values within the range between 1.31 and 1.39 are demonstrated in Fig. 2.5(b), where a good linear relationship with the linearity of 99.9% is obtained. The RI sensitivity obtained is ~994 nm/RIU, which is comparable to that of FPIs reported by other groups [1-3, 7], superior to that of the fiber RI sensors based on fiber Bragg gratings [19, 20], long-period fiber gratings [21] and conventional fiber interferometers [22-24], and much lower than that of the fiber open-cavity MZI, which reaches ~9370 nm/RIU [17]. This is due to the fact that for FPI, the sensitivity is inversely proportional to the RI value of the cavity medium as illustrated in Equitation 2.3, whereas for MZI, it is inversely proportional to the RI difference of the cavity medium and the fiber core, which is much smaller than the RI of the cavity medium itself as illustrated in Equitation:

$$\frac{\Delta\lambda_m}{\Delta n} = \frac{\lambda_m}{n} \tag{2.3}$$

$$\frac{\Delta\lambda_m}{\Delta(n_{eff} - n)} = \frac{\lambda_m}{n_{eff} - n} \tag{2.4}$$

Where n_{eff} is the effective RI of the fiber core.

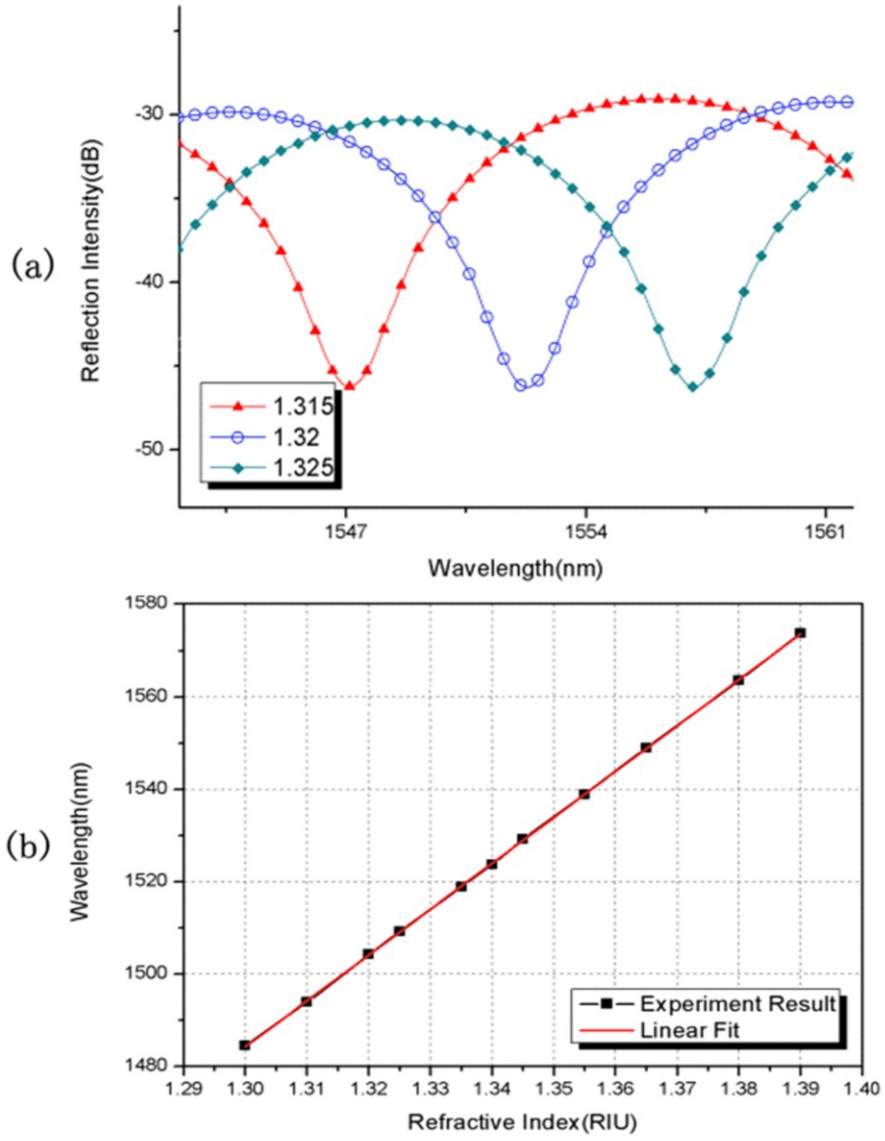

Fig. 2.5 Response of refractive index (a) The reflection spectrum at RI = 1.315, 1.32 and 1.325, respectively (b) RI response of the sensor.

2.2 Thermal Response

The temperature influence on the FPI cavity RI sensor has been investigated by placing the fiber tip in an electrical oven and gradually increasing the temperature from 24 to 100 °C. The temperature sensitivity obtained is ~4.8 pm/°C near the wavelength position of 1554 nm, as shown in Fig. 2.6. Based on the RI sensitivity of ~994 nm/RIU, the temperature cross sensitivity of the sensor is ~4.8 × 10^{-6} RIU/°C, Over the temperature variation of 76°C, the total temperature cross-sensitivity measurement error is as low as~ 3.8×10-4 RIU, which indicated the small temperature dependence of this device.

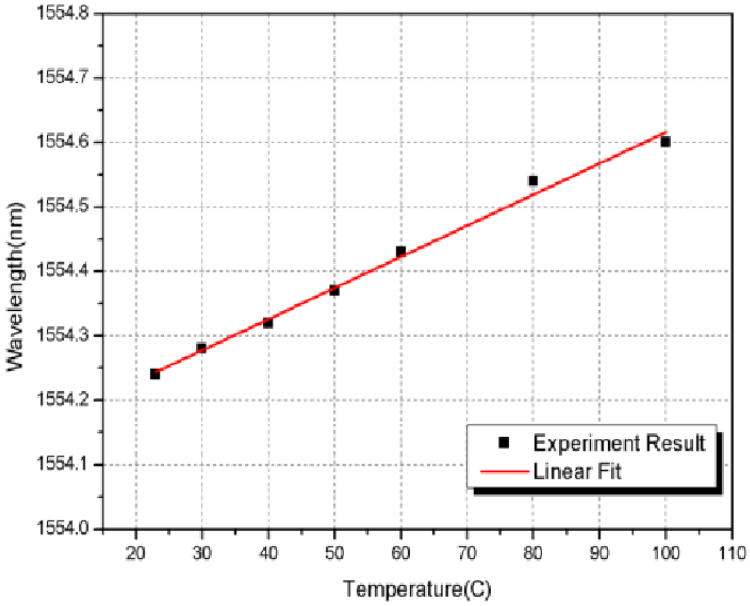

Fig. 2.6 Temperature response of the sensor

2.3 Summary and Discussion

A fiber in-line FPI sensor based on air cavity has been proposed and demonstrated for RI measurement. The change of liquid RI value causes the change of the optical path difference of FPI, which in turn leads to an interference spectrum shift. Then some characteristics of these FPI were discussed in detail, including the fabrication process and the parameters controlling during the process. It is found by controlling

the micro-hole diameter, fusion time and fusion current, air cavities with different size could be obtained. Finally the RI response and thermal response of FPI are experimentally investigated. The RI sensitivity achieved in the experiment is ~994 nm/RIU, and the temperature cross-sensitivity is as low as ~4.8×10^{-6} RIU/°C. Such a device is simple in structure, easy in fabrication and reliable in operation.

However, the mechanism of the fiber in-line FPI is similar to that of the FPI reviewed in chapter 1, and the open air cavity with micro-channel is fragile in structure. In the next chapter, based on air cavity, a MZI based on closed air cavity with novel interference mechanism will be proposed. By changing the position of the microhole on the fiber tip from the centre to the cladding area, an asymmetrical air cavity adjacent to fiber core would be fabricated after similar fabrication process introduced in this chapter. This MZI exhibits highly sensitivity for high temperature and great robustness over open cavity.

Reference

[1] Z. X. Gao, A. Adnet, Z. Zhang et al, "Monitoring changes in the refractive index of gases by means of a fiber optic Fabry-Perot interferometer sensor," Sensors Actuat. A-Phys. 118, 117-182 (2005)

[2] P. Domachuk, I. C. M. Littler, M. Cronin-Golomb et al, "Compact resonant integrated microfluidic refractometer," Appl. Phys. Lett. 88, 093513 (2006)

[3] T. Wei, Y. Han, Y. Li, et al, "Temperature-insensitive miniaturized fiber inline Fabry-Perot interferometer for highly sensitive refractive index measurement," Opt. Express 16, 5764-5769 (2008)

[4] J. Villatoro, V. Finazzi, G. Coviello, et al, "Photonic-crystal-fiber-enabled micro-Fabry-Perot interferometer," Opt. Lett. 34, 2441-2443 (2009)

[5] J. Ma, J. Ju, L. Jin, et al, "Fiber-tip micro-cavity for temperature and transverse load sensing," Opt. Express 19, 12418-12426 (2011)

[6] M. S. Ferreira, L. Coelho, K. Schuster, et al, "Fabry-Perot cavity based on a diaphragm-free hollow-core silica tube," Opt. Lett. 36, 4029-4031 (2011)

[7] Z. Ran, Y. J. Rao, J. Zhang, et al, "A miniature fiber-optic refractive-index sensor based on lasermachined Fabry-Perot interfermmeter tip," J. Lightwave Technol. 27, 5426-5429 (2009)

[8] H. Y. Choi, G. Mudhana, K. S. Park, et al, "Cross-talk free and ultra-compact fiber optic sensor for simultaneous measurement of temperature and refractive index," Opt. Express 18, 141-149 (2010)

[9] K. Mileńko, D. J. Hu, P. P. Shum, et al, " Photonic crystal fiber tip interferometer for refractive index sensing," Opt. Lett. 37, 1373-1375 (2012)

[10] Z. L. Ran, Y. J. Rao, W. J. Liu, et al, "Laser-micromachined Fabry-Perot optical fiber tip sensor for high-resolution temperature-independent measurement of refractive index," Opt. Express 16, 2252-2263 (2008)

[11] K. M. Davis, K. Miura, N. Sugimoto, et al, "Writing waveguides in glass

with a femtosecond laser," Opt. Lett. 21, 1729-1731 (1996)

[12] W. J. Chen, S. M. Eaton, H. Zhang, et al, "Broadband directional couplers fabricated in bulk glass with high repetition rate femtosecond laser pulses," Opt. Express 16, 11470-11480 (2008)

[13] Y. Kondo, K. Nouchi, T. Mitsuyu, et al, "Fabrication of long-period fiber gratings by focus irradiation of infrared femtosecond laser pulses," Opt. Lett. 24, 646-648 (1999)

[14] S. J. Mihailov, C. W. Smelser, P. Lu, et al, "Fiber Bragg gratings made with a phase mask and 800-nm femtosecond radiation," Opt. Lett. 28, 995-997 (2003)

[15] S. J. Liu, L. Jin, W. Jin, et al, "Structural long period gratings made by drilling micro-holes in photonic crystal fibers with a femtosecond infrared laser," Opt. Express 18, 5496-5503 (2010).

[16] M. Park, S. Lee, W. Ha, et al, "Ultracompact intrinsic micro air-cavity fiber Mach-Zehnder Interferometer," IEEE Photon. Technol. Lett. 21, 1027-1029 (2009)

[17] Y. Wang, M. W. Yang, D. N. Wang, et al, "Fiber in-line Mach-Zehnder interferometer fabricated by femtosecond laser micromachining for refractive index measurement with high sensitivity," J. Opt. Soc. Am. B 27, 370-374 (2010)

[18] J. Yang, L. Jiang, S. Wang, et al, "Highly sensitive refractive index optical fiber sensors fabricated by a femtosecond laser," IEEE Photonics J. 3, 1189-1197 (2011)

[19] H. Y. Fu, K. M. Zhou, P. Saffari, et al, "Microchanneled chirped fiber Bragg grating formed by femtosecond laser aided chemical etching for refractive index and temperature measurements," IEEE Photon. Technol. Lett. 20, 1609-1611 (2008)

[20] X. Fang, C. R. Liao, and D. N. Wang, "Femtosecond laser fabricated fiber Bragg grating in microfiber for refractive index sensing," Opt. Lett. 35, 1007-1009 (2010)

[21] V. Bhatia and A. M. Vengsarkar, "Optical fiber long-period grating sensors," Opt. Lett. 21, 692-694 (1996)

[22] J. F. Ding, A. P. Zhang, L. Y. Shao, et al, "Fiber-taper seeded long-period grating pair as a highly sensitive refractive index sensor," IEEE Photon. Technol. Lett. 17, 1247-1249 (2005)

[23]. R. Jha, J. Villatoro, G. Badenes, et al, "Refractometry based on a photonic crystal fiber interferometer," Opt. Lett. 34, 617-619 (2009)

[24] Z. B. Tian, S. S. H. Yam, and H. P. Loock, "Refractive index sensor based on an abrupt taper Michelson interferometer in a single-mode fiber," Opt. Lett. 33, 1105-1107 (2008)

Chapter 3

Miniaturized Fiber In-Line Mach–Zehnder Interferometer Based on Inner Air Cavity for High-Temperature Sensing

Optical fiber sensors have been attractive for high temperature measurement because of its light weight, small size, immunity to electromagnetic interference and remote sensing capability. Many optical fiber high temperature sensors have been proposed; including FBG, LPFG and interferometer based systems [1-11]. Among them, fiber in-line MZI is of particular interests owing to its high sensitivity. A number of MZI structures have been reported such as that based on fiber tapers [9] and fiber core diameter mismatch [10]. However, such structures suffer the drawbacks of large device dimension or poor robustness. Recently, a robust fiber in-line MZI has been used for temperature sensing [12]. In such a device, an inner air cavity with diameter of 10 μm is created to cross over the fiber core area. As one of the interferometer arms supports higher order cladding modes propagating near the fiber surface, excited by the air cavity, the output spectrum varies with the surrounding RI fluctuation. Although only lower order of cladding modes can be excited by use of small air-hole inside the fiber core [13], a pair of similar air-holes needs to be created and separated by a distance of 20 mm, which makes it difficult to the measure the temperature at precise location. Moreover, such a temperature sensor formed exhibits a nonlinear response.

In this chapter, a fiber in-line MZI based on inner air cavity adjacent to the fiber core

is proposed and demonstrated for high temperature sensing at precise location. The air cavity is fabricated by using fs laser micromachining together with fusion splicing technique. Light propagating in the fiber core is divided into two portions: one passing through the air cavity and the other traveling along the fiber core, before recombining at the air cavity end. This sensing theory has been adopted in a open air cavity MZI sensor [11,15], but the closed air cavity structure introduced in this paper exhibits great advantages including higher robustness and lower RI cross-sensitivity over the open cavity structure. Such an MZI is miniature and robust, response linearly to the temperature, with high temperature sensitivity of ~43.2 pm/°C up to 1000/°C while being insensitive to the surrounding RI variation. The operation principle, fabrication process, high temperature response, axial strain response and RI response of the MZI have been investigated in this chapter.

3.1 Operation Principle of Mach–Zehnder Interferometer Based on Inner Air Cavity

Fig. 3.1 shows the schematic structure of the fiber in-line MZI proposed. The inner air cavity adjacent to the fiber core leads to the transition from the fundamental mode to cavity mode and cladding mode. After one micro-machining structure intended to suppress the cladding mode is done, the input light is split into two portions by the air cavity adjacent to the fiber core across a silicon–air interface, denoted by I_{in1} and I_{in2}, respectively. While I_{in1} traveling through the air cavity, I_{in2} remains propagating within the fiber core, and interference happens when the two output beams, I_{out1} and I_{out2} recombine in the fiber core, at the air cavity end. The MZI output intensity can be written as [16]:

$$I = I_{out1} + I_{out2} + 2\sqrt{I_{out1} I_{out2}} \cos\left(\frac{2\pi L \Delta n_{eff}}{\lambda} + \varphi_0\right) \qquad (3.1)$$

where λ is the wavelength of the incident light, L is the air cavity length, $\Delta n_{eff1} = n_{eff}^{core} - n_{eff}^{cavity}$ is the effective RI difference between the core mode and the unguided air cavity mode, and φ_0 is the initial phase of the interference. Assuming that L keeps constant, the temperature sensitivity of the MZI can be derived from Eq. (1) as:

$$\frac{d\lambda}{dT} = \frac{\lambda}{n_{eff}^{core}(T) - n_{eff}^{cavity}(T)}\left(\frac{dn_{eff}^{core}(T)}{dT} - \frac{dn_{eff}^{cavity}(T)}{dT}\right) \quad (3.2)$$

where $\frac{dn_{eff}^{core}(T)}{dT}$ and $\frac{dn_{eff}^{cavity}(T)}{dT}$ are temperature coefficients of the RI of fiber core and air, respectively. Note that n_{eff}^{cavity} remains the same for different temperatures, hence the sensitivity of the MZI is determined by the temperature coefficient of the RI of the fiber core.

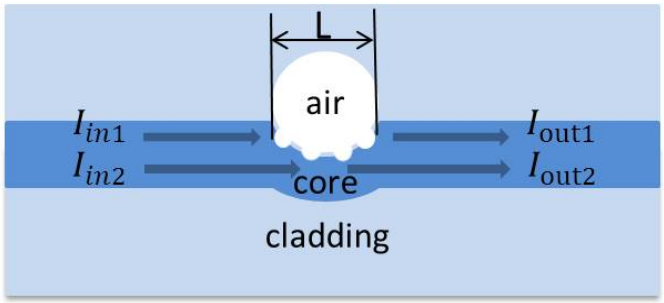

Fig. 3.1. Schematic diagram of the fiber in-line MZI proposed.

However, besides the interference between the leaky mode in the air cavity and the fundamental mode in the fiber core mentioned above, there is an unwanted interference. The mechanism of the unwanted interference illustrated in Fig. 3.2. Part of the input light beam in the fiber core follows path 1, is reflected by the first air spherical cavity surface, and is incident on the interface between the fiber cladding and air, where it experiences another reflection before being reflected again at the

second air spherical cavity surface and returned to the fiber core to continue propagation. The rest of the input light beam in the fiber core propagates along path 2 and recombines with the light beam traveling in path 1 at the end of air spherical cavity surface, thus leading to an unwanted interference. When the phase term satisfies the condition that $2\pi\Delta(nL)/\lambda = (2m+1)\pi$, where m is an integer and $\Delta(nL)$ is the OPD between the two interferometer arms shown in Fig 3.2, the intensity dip appears at the wavelength

$$\lambda_{dip_{unwanted}} = \frac{2\Delta(nL)}{2m+1} \tag{3.3}$$

The FSR of the interference fringe dip of interest is determined by the OPD, $\Delta(nL)$, as

$$FSR_{unwanted} = \frac{\lambda^2}{\Delta(nL)} \tag{3.4}$$

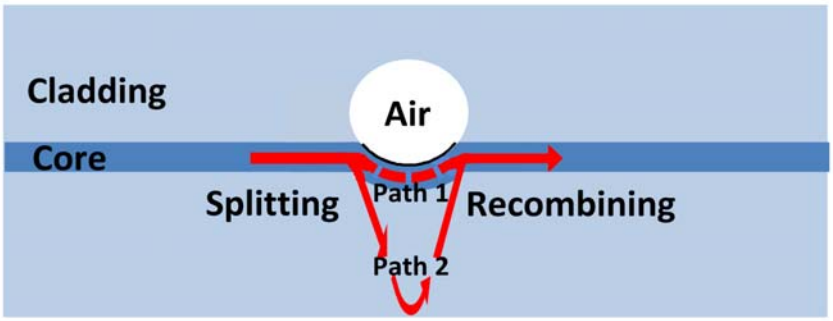

Fig. 3.2. Mechanism of the unwanted interference.

3.2 Fabrication of Mach–Zehnder Interferometer Based on Inner Air Cavity

In the device fabrication, fs laser pulses (λ = 800 nm) of 120 fs at the repetition rate of 1 kHz were focused onto the fiber by a 20× objective lens with an NA value of 0.50 and a working distance of 2.1mm. A CCD camera was employed to monitor the fabrication process and record the sample morphology. A standard SMF-28 with the core diameter of 8.2 μm and the nominal effective RI of 1.4682 (at 1550 nm) was mounted on a computer controlled three dimensional translation stage with a 40-nm resolution.

A micro square structure as shown in Fig. 3.3(a), with the side length of ~20 μm and the largest depth of ~23 μm, centred at 15 μm away from the center of the cleaved fiber end facet, was inscribed by fs laser pulses with the energy of ~3 μJ. The microscope image of the cross section view of the fiber tip with the micro square structure is displayed in Fig. 3.3(b). The fiber tip with micro-structure was then fusion spliced together with another cleaved SMF tip without micro structure to create a hollow sphere adjacent to the fiber core as demonstrated in Fig. 3.3(c), which essentially formed an MZI. Fig. 3.3(d) provides the microscope image of the hollow sphere obtained. The fusion splicer used was ERICSSO FSU975 and the fusing current and fusing duration employed were 14.3 mA and 1.5 s, respectively. It should be noted that besides the fundamental core mode and the air cavity mode, higher order cladding modes are also excited by the air cavity, which lead to multiple beam interference and, as the higher order cladding modes propagate near the fiber surface, the interferometer output is sensitive to surrounding RI variation. To suppress the influence of higher order cladding mode, the micro-structure on the inner surface of the air cavity as shown in Fig. 3.3(e) was fabricated by fs laser

micromachining, which consisted of 4 parallel lines across the air cavity and fiber core boundary. Fig. 3.3(f) and its inset show the microscope image of the side view and the top view of the air cavity with such a micro-structure respectively. In the micro-structure fabrication process, the fs laser pulses with pulse energy of 1.5 μJ were focused onto the air cavity inner surface adjacent to the fiber core and scanned at a speed of 200 μm/s across the fiber diameter, in perpendicular to the fiber axis, to create a micro-line at the edge of the air cavity. The laser beam was then shifted by 10 μm, in parallel to the fiber axis and started a new cycle of scanning until 4 micro-lines were produced on the inner surface of the air cavity. As shown in the inset of Fig. 3.3(f), clear tracks were formed along the scanning paths when the focused laser beam was moving from the air cavity into the silica bulk. This is due to the fact that the surface damage threshold of fused silica at the air-dielectric interface is much lower than that in the bulk [14]. Once the focused beam intensity is lower than the bulk damage threshold but higher than that of the surface, defects are formed in the vicinity of the focal spot when the laser beam crossing the air cavity interface. Such defects lower the local damage threshold of the adjacent materials along the laser scanning path.

The MZI output spectrum corresponding to the air cavity without micro-structure contains two sets of fringes: the one with large FSR is produced by the interference between the core mode and the air cavity mode, and the other with small FSR value of 40 nm is due to interference based on the inner mirrors formed by the surface of the air spherical cavity. The response of MZI fiber sensor is traced by monitoring the dip wavelength shift of the interference between the core mode and the air cavity mode, and the other interference acts as noise. The micro-structure is fabricated to eliminate the unwanted set of interference. Based on the mechanism of the unwanted interference, visibility of the unwanted interference counts significantly on the

smoothness of the air cavity. The microstructure makes the surface rough and unable to reflect the light beam in the fiber core, breaking the condition of reflection at the spherical cavity surface, thus eliminate corresponding interference fringe.

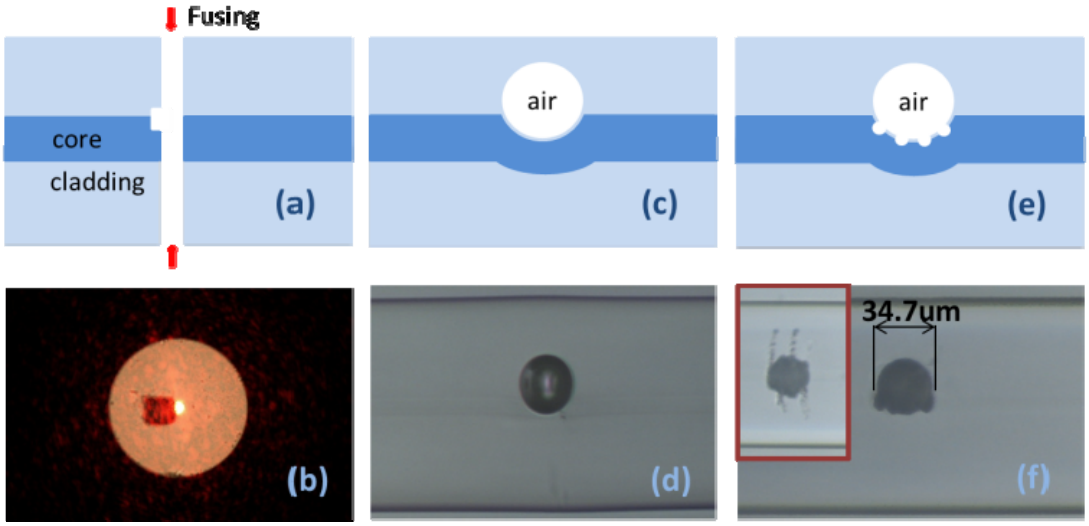

Fig. 3.3. Illustration of the fiber in-line MZI fabrication process. (a) Micro-structure created at the end of fiber tip. (b) Microscope image of the fiber tip with micro-square structure. (c) Air cavity adjacent to the fiber core formed in SMF. (d) Microscope image of the air cavity formed in SMF. (e) The air cavity with micro-structure. (f) Microscope images of the side view and top view (inset) of the air cavity with micro-structure.

The impact of inscribed micro-structure on the inner surface of the air cavity is illustrated in Fig. 3.4. As both the intensities of the air cavity mode and cladding modes are very small when compared with that of the core mode, the interference between the air cavity mode and higher order cladding mode can be ignored. When the micro-structure is introduced on the inner surface of the air cavity, the air cavity surface is not smooth anymore. The visibility of the interference fringe with small FSR decreases significantly and the fright pattern almost disappears. A small dip wavelength shift is observed for the fringe pattern with large FSR, together with a large visibility improvement, due to the fact that part of the core mode is excited into the air cavity mode.

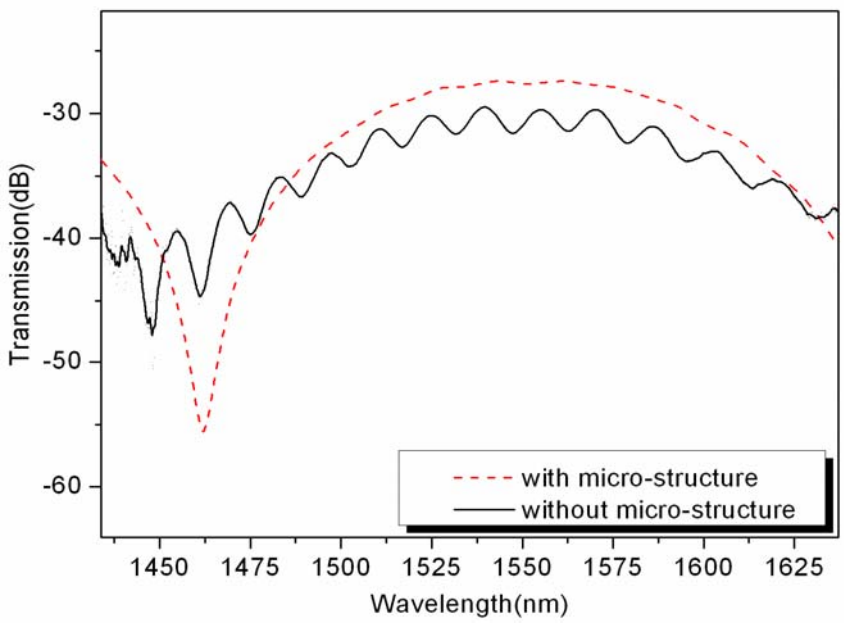

Fig. 3.4. The interference spectrum with or without micro-structure on the inner surface of the air cavity.

3.3 High Temperature Response

The temperature measurement of the device is implemented by use of a tubular furnace. Firstly, the sensor was heated from room temperature (27°C) to 1000°C at an average rate of 5°C/min, and stayed at 1000°C for 3 hours to remove the burnt fiber coating induced effects before being cooled down to room temperature. The temperature was then gradually increased to 100°C, and from 100°C to 1000°C with a step of 100°C, stayed for 20 min at each step. The sensor was kept at 1000°C for half a hour before being cooled down to 100°C, following the same step and staying time as in the heating process. Fig. 3.5(a) shows the transmission spectra at a number of temperature points and a clear red shift of fringe dip wavelength with the increase of temperature can be observed. The fringe dip wavelength shift with the temperature change is displayed in Fig. 3.5(b), where a good repeatability in both the heating and the cooling processes can be found and the temperature sensitivity obtained is ~43.2 pm/°C.

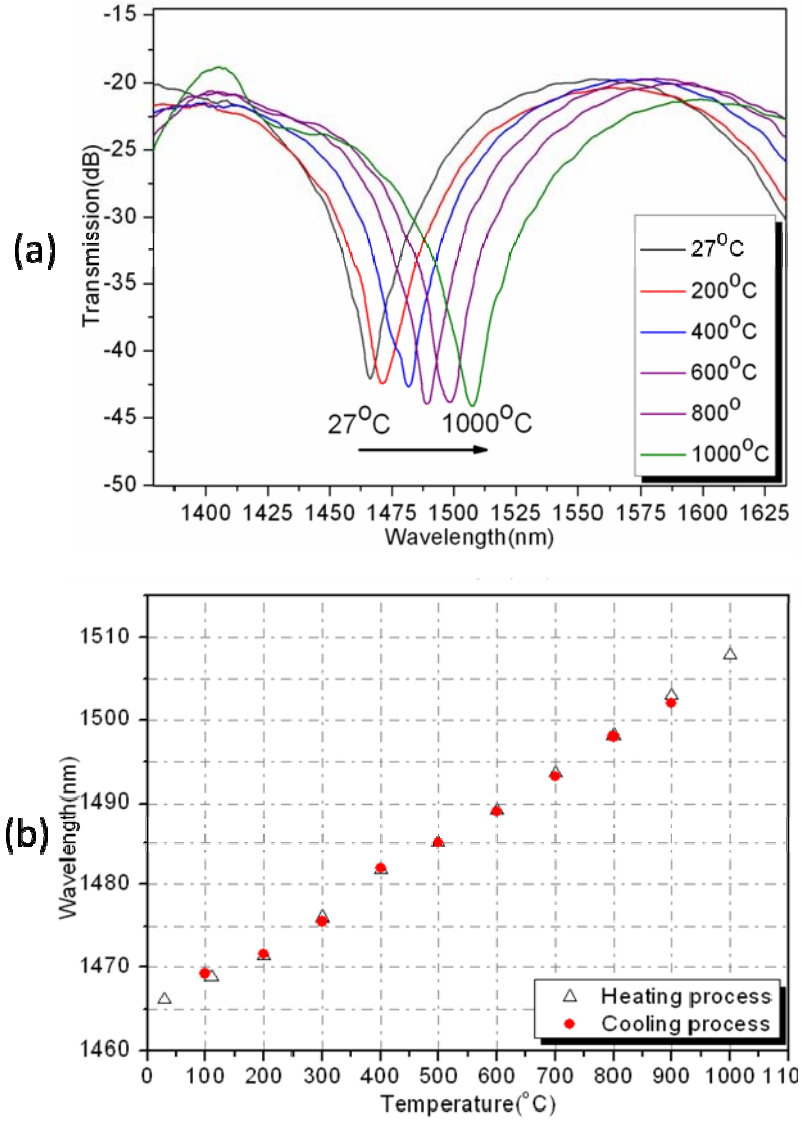

Fig. 3.5. (a) Interference spectra of the fiber in-line fiber MZI at different temperatures.

(b) Interference dip wavelength versus temperature.

3.4 Refractive Index Response

The response of the MZI to the ambient RI change was examined by immersing the device in the liquids with RI values ranging from 1.35 to 1.60. Fig. 3.6 shows the transmission spectra of the MZI in different RI liquids. The nearly unchanged spectrum reveals the

insensitivity of the device to the surrounding RI. This further confirms that the interference happens between the fundamental core mode propagating along the fiber core and the unguided mode passing through the air cavity, as the interference between them would not be influenced by the change of external RI.

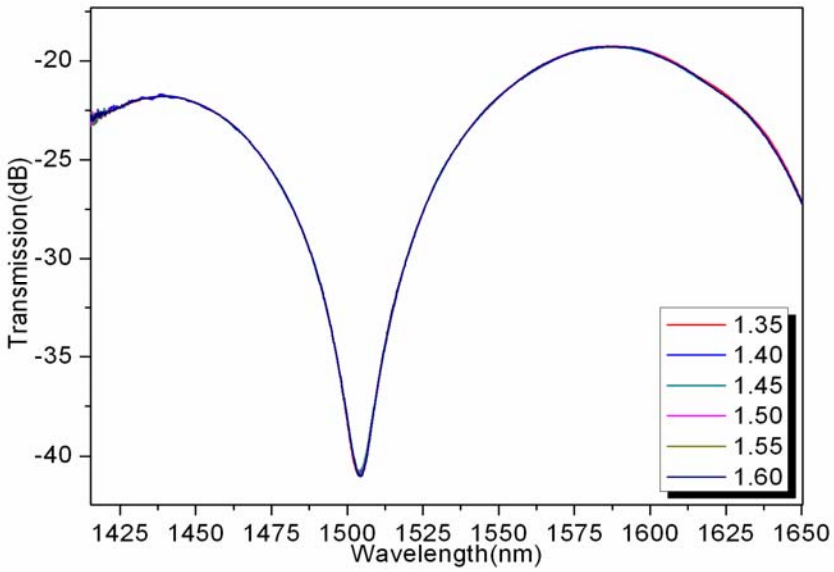

Fig. 3.6 Interference spectra of the in-line fiber MZI immersed in different RI liquids.

3.5 Axial Strain Response

The response of the MZI to the axial strain was also tested in the range between 0 and 3157 με and the results obtained are shown in Fig. 3.7. The strain sensitivity obtained is only ~1.15 pm/με owing to the small inner air cavity in the SMF, which makes the strain cross-sensitivity be small as 0.0266 °C/με. The wide strain measurement range up to 3157 με also indicates the robustness of the device.

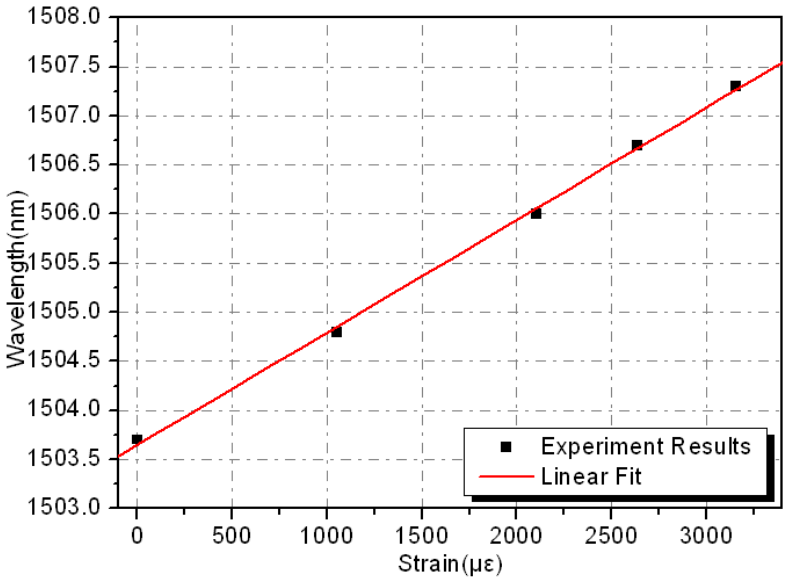

Fig. 3.7 Interference dip shift versus strain.

3.6 Summary and Discussion

In summary, a fiber in-line MZI based on inner air cavity adjacent to fiber core is developed for high temperature sensing. The inner air cavity is fabricated by fs laser micromachining together with fusion splicing technique. The influence of higher cladding mode can be eliminated and hence the RI cross-sensitivity be removed by introducing micro-structure on the inner surface of the air cavity. The device exhibits a high temperature sensitivity of ~43.2 pm/°C up to 1000°C and a small strain cross-sensitivity of ~0.0266 °C/με. The fiber in-line MZI sensor developed is miniature and robust, with high temperature sensitivity and low external RI and strain cross-sensitivities.

In the next chapter, a fiber in-line MZI based on another microstructure will be proposed. The microstructure will be fabricated on the surface of an air cavity inside the fiber by similar method, but the fs laser intensity would be adjusted higher and the irradiation time longer. Different from the microstructure eliminating the unwanted interference in this chapter, the one in the next chapter will converts part of the incident light beam into

cladding mode. A hydrogen sensor will be demonstrated based on that structure in the Chapter 4.

Reference

[1] G. Brambilla and H. Rutt, “Fiber Bragg gratings with enhanced thermal stability,” Appl. Phys. Lett. 80, 3259-3261 (2002)

[2] D. Grobnic, C. W. Smelser, S. J. Mihailov, et al, “Long-term thermal stability tests at 1000^{o}C of silica fiber Bragg gratings made with ultrafast laser radiation,” Meas. Sci. Technol. 17, 1009-1013 (2006)

[3] Y. Li, M. Yang, C. R. Liao, D. N. Wang, et al, “Prestressed fiber Bragg grating with high temperature stability”, IEEE J Lightwave Technol. 29, 1555-1559 (2011)

[4] V. Bhatia and A. M. Vengsarkar, “Optical fiber long-period grating sensors,” Opt. Lett. 21, 692-694 (1996)

[5] S. Bandyopadhyay, J. Canning, M. Stevenson, et al, “Ultrahigh-temperature regenerated gratings in boron-co doped germanosilicate optical fiber using 193 nm,” Opt. Lett. 33, 1917-1919 (2008)

[6] Y. Zhu, P. Shum, H. Bay, et al, “Strain-insensitive and high-temperature long-period gratings inscribed in photonic crystal fiber,” Opt. Lett. 30, 367-369 (2005)

[7] Y. Zhu, Z. Huang, F. Shen, et al, “Sapphire-fiber-based white-light interferometric sensor for high-temperature measurements,” Opt. Lett. 30, 711-713 (2005)

[8] H. Y. Choi, K. S. Park, S. J. Park, et al, "Miniature fiber-optic high temperature sensor based on a hybrid structured Fabry-Perot interferometer," Opt. Lett. 33, 2455-2457 (2008)

[9] D. Monzón-Hernández, V. P. Minkovich, and J. Villatoro, “High-temperature sensing with tapers made of microstructured optical fiber,” IEEE Photon.

Technol. Lett. 18, 511-513 (2006)

[10] L. V. Nguyen, D. Hwang, S. Moon, et al, “High temperature fiber sensor with high sensitivity based on core diameter mismatch,” Opt. Express, 16, 11369-11375 (2008)

[11] Y. Wang, Y. Li, C. Liao, D. N. Wang, et al, “High-Temperature Sensing Using Miniaturized Fiber In-Line Mach-Zehnder Interferometer,” IEEE Photon. Technol. Lett. 22, 39-41 (2010)

[12] M. Park, S. Lee, W. Ha, et al, “Ultracompact intrinsic micro air cavity fiber Mach-Zehnder interferometer”, IEEE Photonics. Technol. Letters, 21, 1027-1029 (2009)

[13] L. Jiang, J. Yang, S. Wang, et al, "Fiber Mach–Zehnder interferometer based on microcavities for high-temperature sensing with high sensitivity," Opt. Lett. 36, 3753-3755 (2011)

[14] C. B. Schaffer, A. Brodeur, and E. Mazur, “Laser-induced breakdown and damage in bulk transparent materials induced by tightly-focused femtosecond laser pulses,” Meas. Sci. Technol. 12, 1784 (2001)

[15] Ying Wang, Minwei Yang, D. N. Wang, et al, "Fiber in-line Mach–Zehnder interferometer fabricated by femtosecond laser micromachining for refractive index measurement with high sensitivity," J. Opt. Soc. Am. B, 27 370-374 (2010)

[16] P. Domachuk, C. Grillet, V. Ta’eed, et al, “Microfluidic interferometer,” Appl. Phys. Lett. 86, 024103 (2005)

Chapter 4

Miniature Hydrogen Sensor Based on Fiber Inner Air-Cavity with Micro-structures

Hydrogen is one of the most important future energy sources owing to its high power efficiency, cleanness (it does not produce any CO_2), sustainability and abundant availability. Currently, hydrogen has been used in many industrial sectors such as aerospace rockets, fuel cells in automobiles, petroleum exploration, chemical processing, welding and power generation. However, safe transportation and control of hydrogen is always a great concern due to its high diffusivity, low ignition energy and wide explosion concentration range (with lower explosive limit of 4% and upper explosive limit of 75%). Thus, the detection of the hydrogen concentration and prevention of its leakage are crucially important. Among various types of hydrogen sensors developed so far, optical fiber sensors are particularly attractive because of their outstanding properties such as intrinsic safety from spark, elevated working temperature, immunity to electromagnetic interference and remote sensing capability [1-3]. To date, optical fiber hydrogen sensors are mainly operated on intensity, interferometric and fiber grating based schemes, and the sensing materials typically used are Pd and its composite film because of their high sensitivity and good selectivity to the gas [1-10]. Recently, fiber in-line interferometers based on open air-cavity coated with Pd film and fabricated by fs micromachining have been demonstrated for hydrogen sensing [11], with ultra compact size and high sensitivity. However, the price paid is its inherently poor robustness.

In this chapter, a Pt-doped WO_3 composite coated fiber device based on fiber inner air-cavity with periodical microstructures is proposed and demonstrated for hydrogen sensing. The fiber inner air-cavity is fabricated by use of femtosecond laser micromachining together with fusion splicing technique while the periodical microstructures are inscribed by fs beam scanning. Such a device is compact and exhibits a high sensitivity as well as a low temperature cross-sensitivity. Moreover, the robustness of the device is also improved compared with that reported in [11], due to the inner structure adopted. Principle and fabrication process of the hydrogen sensor is described, and hydrogen response and thermal response have been investigated.

4.1 Operation Principle of Miniature Hydrogen Sensor Based on Fiber Inner Air-Cavity with Microstructures

The schematic diagram of the device is shown in Fig. 4.1. The inner air-cavity adjacent to the fiber core exhibits periodic microstructures on the cavity surface and hence introducing a structure modulation on the fiber core, which converts part of the incident light beam on the cavity into cladding mode, while the rest remain travels along the fiber core and as a result, loss dips appear in the transmission spectrum. Fig. 4.2 and its insets demonstrate the transmission spectra and the microscope image of the side view and the top view of the two samples of fiber inner air-cavity with microstructures, respectively. The microstructures in the two samples possess the same period of 5μm, which leads to the similar transmission spectra and nearly the same dip wavelengths located at 1573nm and 1607nm, respectively. This microstructure is fabricated by similar methods as that in chapter 3, but other than

that in chapter 3, the fiber core is partly damaged by this microstructure. The periodic microstructure device proposed in this chapter is similar to the micro-hole structured LPFG [12], however, with a smaller number of period and more compact size.

After being coated with Pt-doped WO_3, a metal compound that can undergo an exothermic reaction with hydrogen, the device can serve as an effective hydrogen leak sensor. The chemical reaction between hydrogen and WO_3 is described as [1]:

$$\begin{aligned} WO_3 + xH_2 &\rightarrow WO_{3-x} + xH_2O \\ WO_{3-x} + \frac{x}{2}O_2 &\rightarrow WO_3 \end{aligned} \tag{4.1}$$

During the reaction process, the refractive index and the absorption of the metal compound are changed, resulting in a shift of output dip wavelength of the WO_3 coated fiber device. Although the reaction released energy elevates the temperature at the fiber location with sol-gel, the device has much smaller sensitivity to the temperature than to the surrounding refractive index.

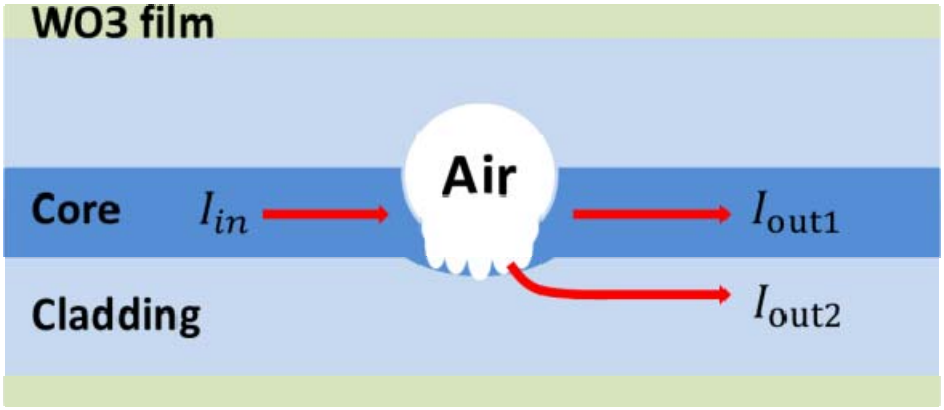

Fig.4.1. Schematic diagram of the hydrogen sensor.

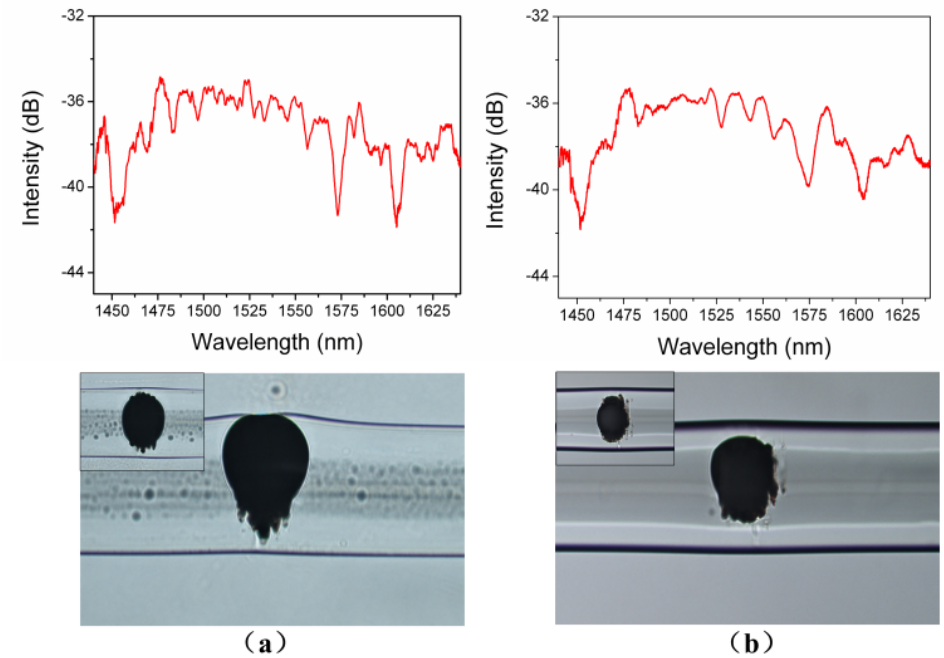

Fig. 4.2. (a) Spectrum and microscope image of side view (inset: top view) of sample 1; (b) spectrum and microscope image of side view (inset: top view) of sample 2.

4.2 Fabrication of Miniature Hydrogen Sensor Based on Fiber Inner Air-Cavity with Microstructures

The fiber inner cavity was fabricated by use of fs micromachining together with the fusion splicing technique [13]. Fs pulses (λ= 800 nm) of 120 fs at the repetition rate of 1 kHz were focused onto the fiber by a 40× objective lens with an NA value of 0.66 and a working distance of 1.7 mm. A CCD camera was employed to monitor the fabrication process and record the sample morphology. A standard SMF with the core diameter of 8.2 μm and the nominal effective refractive index of 1.4682 (at 1550 nm) was mounted on a computer controlled three dimensional translation stage with a 40-nm resolution. A micro-circle structure with a diameter of ~28 μm and the largest depth of ~30 μm, centered at 18 μm away from the center of the cleaved fiber end facet, was inscribed by fs pulses with energy of ~1.5 μJ. The fiber tip with

microstructure was then fusion spliced together with another cleaved SMF tip without microstructure to create a fiber inner cavity adjacent to the fiber core. The fusion splicer used was ERICSSO FSU975, and the fusing current and fusing duration employed were 15.2 mA and 2.0 s, respectively. The microstructure on the surface of the inner cavity was fabricated by fs micromachining, which consisted of a number of parallel lines across the inner cavity. In the microstructure fabrication process, the fs pulses with pulse energy of 1.5 μJ were focused onto the cavity inner surface adjacent to the fiber core and scanned with a speed of 100 μm/s from one side of the fiber to the other, perpendicular to the fiber core axis, thus creating a channel at the edge of the cavity. After completion of one scanning, the laser beam was shifted by 5 μm, in parallel to the fiber until line shape structures with 9 channels on the inner surfaces were inscribed. To prepare the first sample shown in Fig. 4.2(a), the scanning procedure was repeated for 7 times, while for the second sample shown in Fig. 4.2(b), only 5 times were repeated. This leads to different levels of modulation intensities, and hence the depths of dip wavelengths. The sample with stronger modulation exhibits larger dip wavelength depth (~4.7dB at 1573nm and ~4.0dB at 1607nm) as shown in Fig. 4.2(a), and that of the sample with weaker modulation exhibits smaller dip wavelength depth (~3.21dB at 1573nm and ~2.28dB at 1607nm) as shown in Fig. 4.2(b).

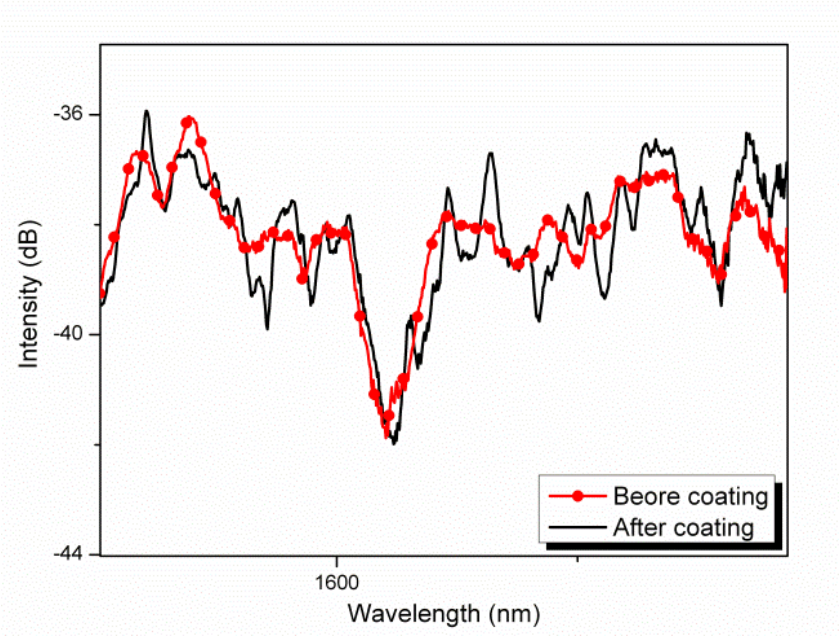

Fig. 4.3. Spectrum before and after coating WO_3-Pd on fiber surface.

The hydrogen sensitive material was prepared using the sol-gel method. Firstly, aqueous sol-gel of H_2WO_4 was obtained from Na_2WO_4 with cation-exchange resin. The solution was washed and centrifuged several times with de-ionized water. Then, appropriate amounts of H_2PtCl_6 $6H_2O$ was mixed with above obtained solution and stirred several hours by magnetic stirrer. Finally, the mixture was annealed at 400 °C for one hour, and the Pt-doped WO_3 powder was prepared. To obtain the sensitive layer, the sensor head was coated with sol-gel WO_3. Around 0.02 g WO_3 powder was smashed with one drop of de-ionized water under ultrasonic oscillation for 10 minutes, before being mixed with de-ionized water. The sensor head was immersed into the solution shortly and then taken out to dry in air for 2 hours, at the temperature of 25 °C. Fig. 4.3 shows the spectra of the device before and after coating.

4.3 Hydrogen Response

In the hydrogen sensing experiment, the sensor head was kept inside a sealed chamber at room temperature and exposed to hydrogen concentrations ranging from 0 to 4% in volume percentage. The dip wavelength shift with the hydrogen concentration is demonstrated in Fig. 4.4, where the inset shows the transmission spectra near 1606 nm, corresponding to different hydrogen concentrations. The dip wavelength is found to experience a blue shift when hydrogen concentration increased. When the hydrogen concentration is increased to 2% in volume percentage, the dip wavelength shift of the device is ~1.13 nm, and in the case of 4%, the dip wavelength shift is ~2.64 nm (i.e. the hydrogen sensitivity is ~660 pm/%), which is more than two orders higher than that of Pd/WO_3 composite coatedFBG [10], as well as with a largely reduced device size.

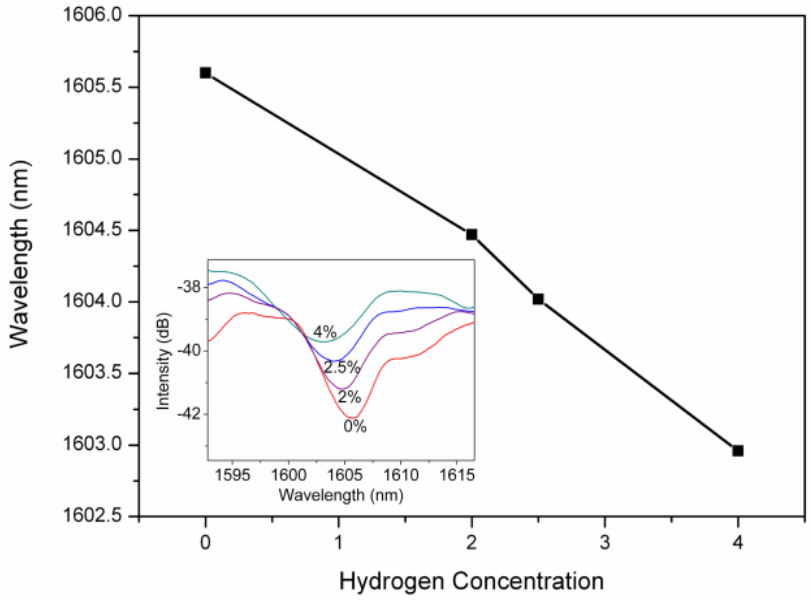

Fig. 4.4. Dip wavelength shift with H_2 concentration. Inset shows the transmission spectra of the device at different H_2 concentration.

Fig. 4.5 displays the dip wavelength response of the device under different hydrogen concentrations. It can be seen from this figure that the device possesses reversible response to the hydrogen of different concentrations. The fringe dip wavelength cannot restore to its initial value, which is likely due to the hysteresis effect of hydrogen recovery in the sensitive coating. Nevertheless, a clear response to hydrogen concentration is demonstrated. The response time is measured to be ~120 s when the device is exposed to 2% of concentration of hydrogen.

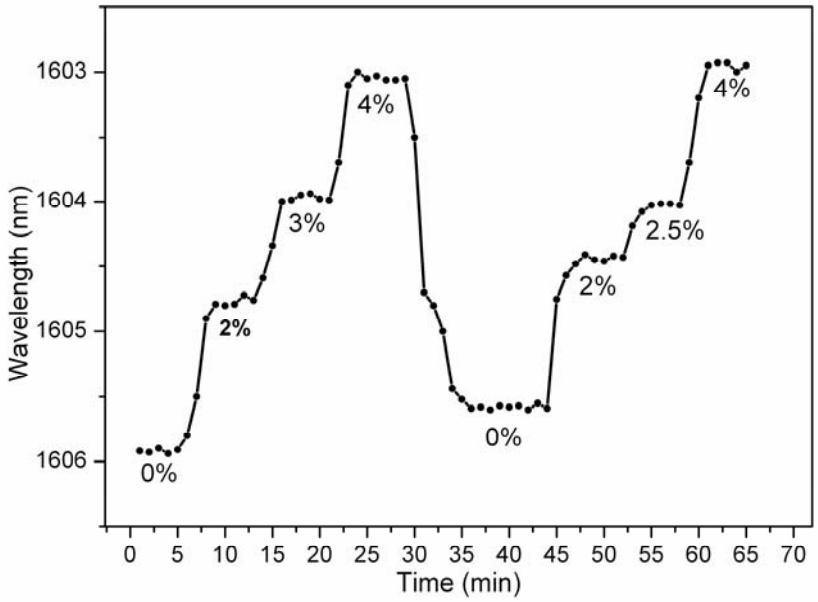

Fig. 4.5. Transmitted intensity changes as a function of H_2 concentration

The sensitivity of the device to hydrogen concentration is primarily due to the RI change of the metal compound with the hydrogen concentration. Refractive index of the proposed sol-gel WO_3 will increase when exposed to hydrogen. Fig. 6 displays the results of the device response to the surrounding RI, and the insets of the figure shows the transmission spectra near 1607 nm, at the RI value of 1.3, 1.32 and 1.34, respectively. A blue shift of dip wavelength indicts that the RI sensitivity of the device is ~-129nm/RIU. Such a device has a large RI sensitivity than that of conventional LPFG, owing to the fact that the modulation is much stronger than that

of the conventional LPFG and that the periodical microstructures are located near the cladding and hence the higher order cladding modes are easily excited.

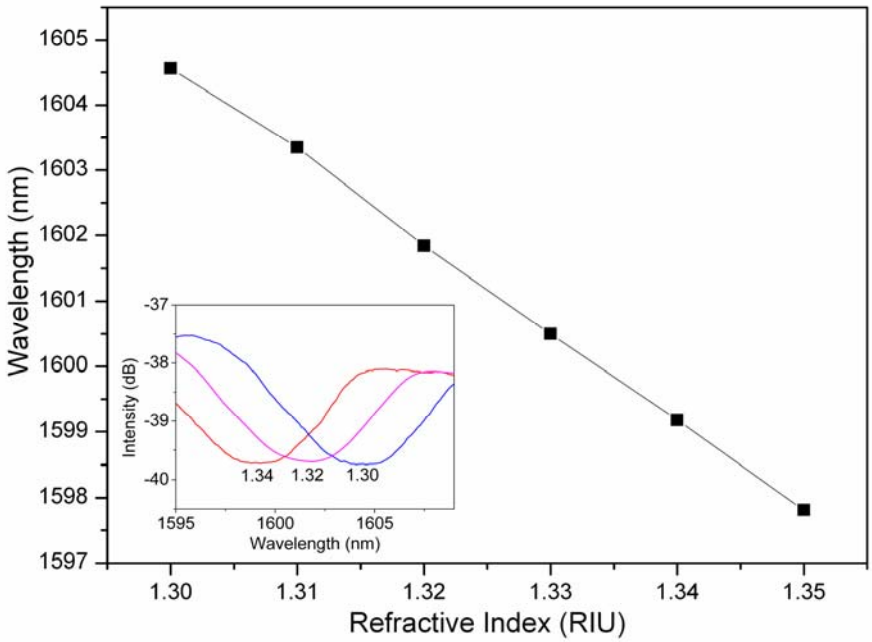

Fig. 4.6. Dip wavelength shift with RI. Inset shows the transmission spectra of the device at different RIs.

4.4 Thermal Response

The temperature effect on dip wavelength shift is demonstrated in Fig. 4.7, where the inset shows the transmission spectra near 1607 nm, at the temperature of 30, 50 and 70^{o}C, respectively. A clear red shift of dip wavelength can be observed and the temperature sensitivity obtained is ~10 pm/^{o}C. Considering the hydrogen sensitivity of ~660 pm/% of the device, temperature cross-sensitivity as low as 0.0152 %/ ^{o}C is achieved.

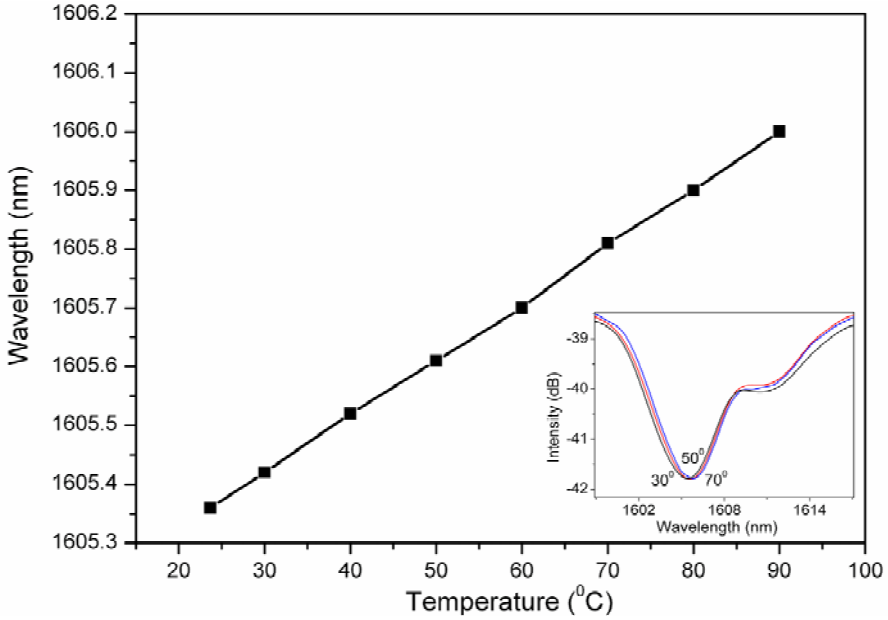

Fig. 4.7. Dip wavelength shift with temperature. Inset shows the transmission spectra of the device at different temperatures.

.

4.5 Summary and Discussion

In conclusion, a miniaturized Pt-doped WO_3 coated fiber device based on microstructures on fiber inner air-cavity is demonstrated for hydrogen concentration sensing. The microstructures convert part of the incident light beam into cladding mode, while the rest remain travels along the fiber core and as a result, loss dips appear in the transmission spectrum. The periodic microstructural device is sensitive to surrounding RI. Coated with Pt-doped WO3 composite, whose RI is changed through the variation of hydrogen concentration, this optical device could work as hydrogen sensor. The maximum wavelength shift is 2.64 nm when the hydrogen concentration is changed from 0 to 4%. The system is highly sensitive, miniature and has a low temperature cross-sensitivity.

In chapter 3 and chapter 4, there are unwanted interference fringes based on the inner

mirrors and microstructures are fabricated to suppress these unwanted interferences. At the meantime, we are trying to design a structure to enhance such interference based on inner mirrors and fabricate a fiber sensor based the interference. In the next chapter, we will report a fiber MZI based on inner mirrors formed by a dual spherical cavity structure, which could perform simultaneously sensing. This MZI is compact in size, robust in mechanical strength, capable for simultaneous sensing temperature, curvature and RI, and free of crosstalk.

Reference

[1] G. Orellana and D. Haigh, “New trends in fiber-optic chemical and biological sensors,” Current Analytical Chemistry, l4, 273-295 (2008)

[2] T. Hubert, L. Boon-Bret, G. Black, et al, “Hydrogen sensors- a review,” Sens. Actuators B Chem., 157, 329-352 (2011)

[3] S. F. Silva, L. Coelho, O. Frazao, et al, “A review of palladium-based fiber-optic sensors for molecular hydrogen detection,” IEEE sensors J., 12, 93-102 (2012)

[4] J. Villatoro and D. Monzon-hernandez, “Fast detection of hydrogen with nano-fiber tapers coated with ultra thin palladium layers,” Opt. Express, 13, 5087-5092 (2005)

[5] C. Caucheteur, M. Debliquy, D. Lahem, et al, “Hybrid fiber gratings coated with a catalytic sensitive layer for hydrogen sensing in air,” Opt. Express, 16, 16854-16859 (2008)

[6] D. Monzon-hernandez, D. Luna-Morena, D. Martinez-Escobar, “Fast response fiber optic hydrogen sensor based on palladium and gold-nano-layers,” Sens. Actuators B Chem., 136, 562-566 (2009)

[7] C. Ma and A. Wang, “Optical fiber tip acoustic resonator for hydrogen sensing,” Opt. Lett., 35, 2043-2045 (2010)

[8] Y. H. Kim, M. J. kim, B. S. Rho, et al, “Ultra sensitive fiber-optic hydrogen sensors based on high order cladding mode,” IEEE sensors J., 11, 1423-1426 (2011)

[9] M. Yang, H. Liu, D. Zhang. X. Tong, “Hydrogen sensing performance comparison of Pd layer and Pd/WO_3 composite thin film coated on side-polished single-and multimode fibers,” Sensors Actuators B Chem., 149, 161-164 (2010)

[10] J. Dai, M. Yang, Y. Chen, et al, "Side-polished fiber Bragg grating hydrogen sensor with Pd/WO_3 composite film as sensing materials," Opt. Express, 19, 6141 (2011)

[11] Min Wang, Minghong Yang, Jie Cheng, et al, "Femtosecond Laser Fabricated Micro Mach-Zehnder Interferometer with Pd film as Sensing Materials for Hydrogen Detection," Opt. Lett., 37, 1940-1942 (2012)

[12] Y. Wang, D. N. Wang, Minwei Yang, et al, "Asymmetric microhole-structured long-period fiber gratings," Sensors Actuators B Chem., 160, 822-825 (2011)

[13] T. Y. Hu, Y. Wang, C. R. Liao, et al, "Miniaturized fiber in-line Mach–Zehnder interferometer based on inner air cavity for high-temperature sensing," Opt. Lett. 37, 5082-5084 (2012)

[14] R. Ghosh, M.B. Baker, R. Lopez, "Optical properties and aging of gasochromic WO_3," Thin Solid Films 518, 2247-2249 (2010)

Chapter 5

Mach–Zehnder Interferometer Based on Dual Internal Mirrors Formed by an Air Spherical Cavity Pair

As introduced in chapter 3, for conventional MZIs, interference is produced by the fiber core mode and cladding mode, propagating along nearly the same path length. The size of the interferometer is usually large owing to the small RI difference between the fiber core mode and the cladding mode, especially when a small free spectral range is required to improve the sensitivity. In order to reduce the size of MZI, we developed an ultra-compact core-air-mode MZI in chapter 3 by use of the inner air cavity adjacent to the fiber core, whose length is below 50 μm due to the large RI difference between the fiber core mode and the air cavity mode. However, the isolated inner cavity structure limits its response to environmental variations such as the surrounding RI change.

In this chapter, we would propose another structure to obtain a compact MZI- the MZI based on dual internal mirrors formed by air spherical cavity surfaces adjacent to the fiber core. The operation principle of this MZI is similar to that of the unwanted interference illustrated in chapter 3. However, the two inner mirrors of this MZI are provided by two separated air spherical cavities, respectively. One of its interesting features is that a compact device size corresponds to a large OPD introduced by the interferometer and hence a small FSR. Moreover, as one of the interferometer arms reaches the air–cladding interface, sensitive response to the

environmental variations can be achieved. What's more, this MZI could perform simultaneous sensing for RI, temperature and curvature and is free of crosstalk. The operation principle, fabrication process, responds of axial, RI, temperature and curvature, and polarization analysis of this MZI have been investigated in this chapter.

5.1 Operation Principle of Mach–Zehnder Interferometer Based on Dual Internal Mirrors

The operation principle of the MZI is illustrated in Fig. 5.1. Part of the input light beam in the fiber core follows path 1, is reflected by the first air spherical cavity surface, and is incident on the interface between the fiber cladding and air, where it experiences another reflection before being reflected again at the second air spherical cavity surface and returned to the fiber core to continue propagation. The rest of the input light beam in the fiber core propagates along path 2 and recombines with the light beam traveling in path 1 at the second air spherical cavity surface, thus forming a fiber in-line MZI. In order to ensure a good interference fringe visibility and low insertion loss, total internal reflection needs to be achieved at every reflection surface described above.

The output intensity of the MZI is governed by

$$I = I_1 + I_2 + 2\sqrt{I_1 I_2}\cos(\frac{2\pi\Delta(nL)}{\lambda}) \tag{5.1}$$

where I_1 and I_2 represent the light intensity at the two interferometer arms, respectively, λ is the wavelength, and $\Delta(nL)$ is the OPD between the two interferometer arms. When the phase term satisfies the condition of $2\pi\Delta(nL)/\lambda = (2m+1)\pi$, where m is an integer, the intensity dip appears at the

wavelength

$$\lambda_{dip} = \frac{2\Delta(nL)}{2m+1} \tag{5.2}$$

The FSR of the interference fringe dip of interest is determined by the OPD, $\Delta(nL)$, as

$$FSR = \frac{\lambda^2}{\Delta(nL)} \tag{5.3}$$

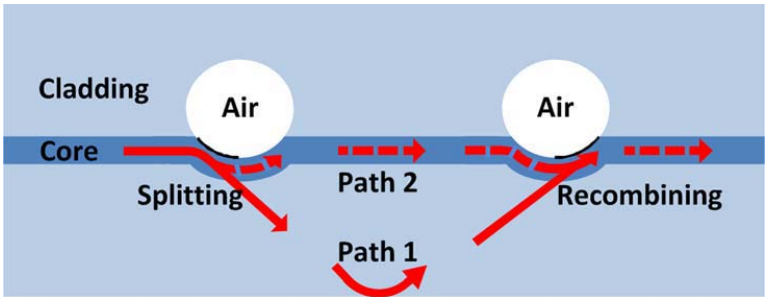

Fig. 5.1. Schematic diagram of the fiber in-line MZI.

5.2 Fabrication of Mach–Zehnder Interferometer Based on Dual Internal Mirrors

The air spherical cavity is fabricated by use of fs laser micromachining, instead of chemical etching, together with the fusion splicing technique. The fs laser pulses (λ=800 nm) of 120 fs at a repetition rate of 1 kHz were focused onto the fiber by a 40× objective lens with an NA value of 0.66 and a working distance of 1.7 mm. A CCD camera was employed to monitor the fabrication process. A standard SMF-28 with effective RI of 1.4682 (at 1550 nm) was mounted on a computer controlled three-dimensional translation stage with 40 nm resolution. A micros quare structure with a side length of ~22 μm and a largest depth of ~35 μm, centered at 20 μm away from the center of the cleaved fiber end facet, was inscribed by fs laser pulses with

energy of ~3 μJ. The fiber tip with microstructure was then fusion spliced together with another cleaved SMF tip without microstructure to create an air spherical cavity adjacent to the fiber core. The fusion splicer used was ERICSSO FSU975, and the fusing current and fusing duration employed were 16.2 mA and 2.0 s, respectively. With the help of a 20× microscope lens together with a CCD camera, the length of the fiber tip near the air spherical cavity end could be controlled before being cleaved. The two fabricated fiber tips with an air spherical cavity were fusion spliced together to form a fiber in-line MZI.

The microscope images of the in fiber air spherical cavity pairs with different separations are demonstrated in Fig. 5.2, together with their corresponding transmission spectra. It can be seen from this figure that the FSR of the device depends on the separation of the air spherical cavity pair and an increased separation leads to an enlarged FSR.

As illustrated in the inset of Fig. 5.2.(f), assuming that the separation of the air spherical cavity pair is 2x, the distance between the fiber central axis and the air-cladding interface is y, then the OPD between the two arms of the interferometer is $\Delta(nL) = 2(n_{cl}z - n_{co}x)$,, where n_{cl} and n_{co} are the RI of fiber cladding and core respectively, and $z = \sqrt{x^2 + y^2}$. When the separation is increased by 2x, the induced OPD change will be approximately $2(n_{cl}\Delta z - n_{co}\Delta x) = 2n_{cl}\Delta x(\frac{\Delta z}{\Delta x} - \frac{n_{co}}{n_{cl}})$.

Since $\frac{\Delta z}{\Delta x} = \frac{x}{z} < 1$, then $(\frac{\Delta z}{\Delta x} - \frac{n_{co}}{n_{cl}}) < 0$, when the air spherical cavity separation is increased, the OPD is decreased, resulting in an enlarged FSR.

The FSR obtained in the experiments are displayed in Fig. 5.2. When compared with

the theoretical curve shown in the same figure, a good agreement can be obtained, which verifies the operation of the MZI developed.

For the fiber in-line MZI reported so far, a relatively large cavity length is needed to produce a small FSR in order to improve the measurement accuracy, which results in a relatively large size of the device. It is interesting to notice that to obtain a small FSR in our device, the separation of the air spherical cavity pair should be reduced, i. e. a more compact device size can be realized, when compared with other fiber in-line MZIs.

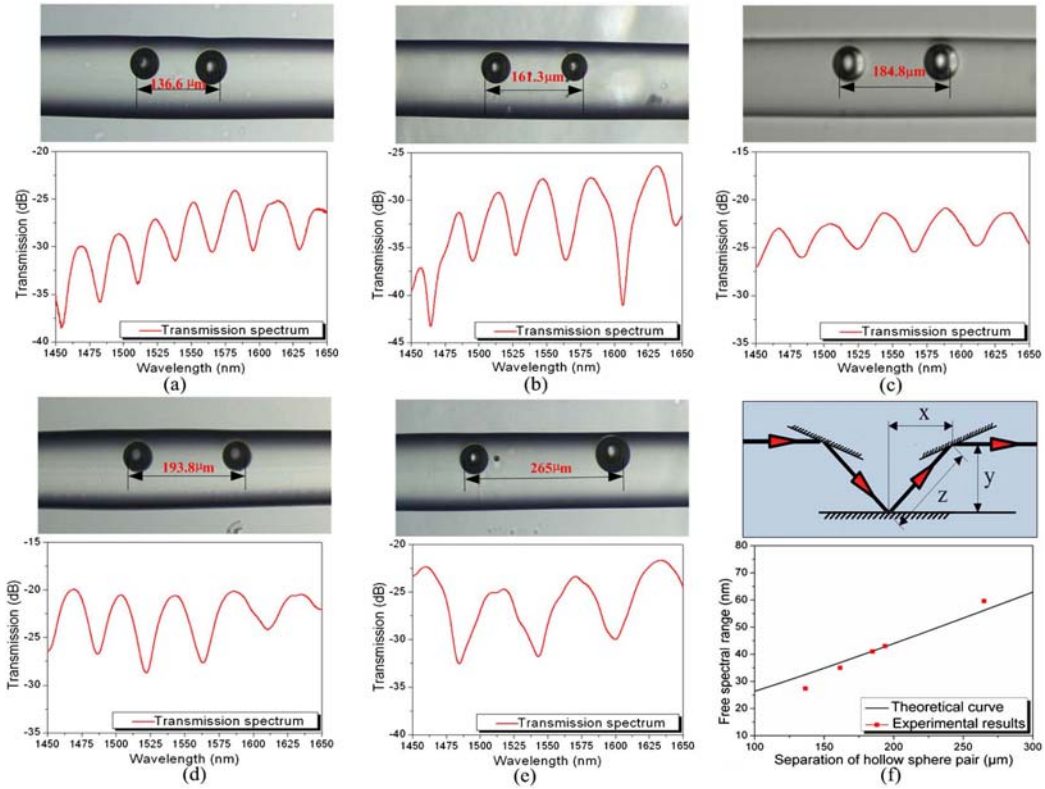

Fig. 5.2. Microscope image and corresponding spectrum for the air spherical cavity pair with separation of (a) 136.6 μm, (b) 161.3 μm,(c) 184.8 μm, (d) 193.8 μm, and (e) 265 μm. (f) FSR versus the separation of the air spherical cavity pair. Inset shows the path of the light reflected by the air spherical cavity pair.

5.3 Axial Strain Response

In the axial strain measurement, the device sample with an air spherical cavity separation of 193.8 $\mu\varepsilon$ was fixed on two translation stages. The dip wavelengths near 1523 nm in the transmission spectra corresponding to different axial strain values are displayed in the inset of Fig. 5.3(a), where a blue shift of fringe dip wavelength appears. Fig 5.3(b) shows the variation of dip wavelength with the axial strain in the range between 0 and 2700 $\mu\varepsilon$, where the sensitivity obtained is −1.44 pm／ $\mu\varepsilon$, which is slightly higher than that of the fiber Bragg grating (FBG) [1,2]—however, with a largely reduced device size. The wide strain measurement range up to 2700 $\mu\varepsilon$ also indicates the robustness f the device. From Eq. (2), we have $\lambda_{dip} = \frac{2\Delta(nL)}{2m+1} = \frac{4}{2m+1}(n_{cl}z - n_{co}x)$, the dip wavelength shift due to the change of axial strain can then be expressed as

$$\begin{aligned}\delta\lambda_{dip} &= \frac{4}{2m+1}[(n_{cl}+\delta n)(z+\Delta z)-(n_{co}+\delta n)(x+\Delta x)]-\frac{4}{2m+1}(n_{cl}z-n_{co}x)\\ &\approx \frac{4}{2m+1}(n_{cl}\Delta z + z\delta n - n_{co}\Delta x - x\delta n) = \frac{4}{2m+1}[n_{cl}\Delta x(\frac{x}{z}-\frac{n_{co}}{n_{cl}})+(z-x)\delta n]\end{aligned} \tag{5.4}$$

where δn is the RI change induced by the increased axial strain and has a negative value. Since $\frac{x}{z}-\frac{n_{co}}{n_{cl}} < 0$, an increase of axial strain would result in a blue shift of the dip wavelength.

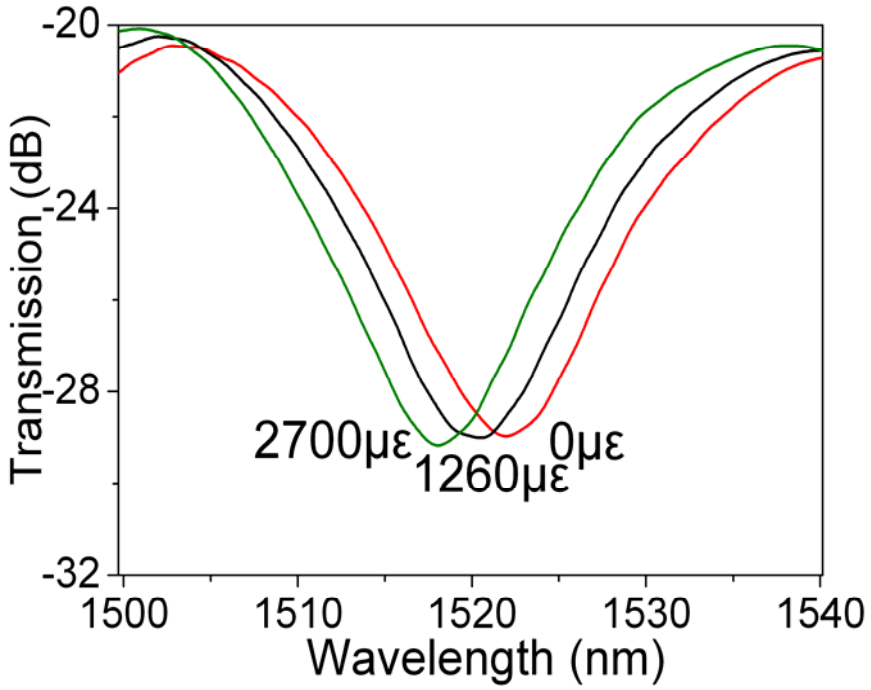

(a)

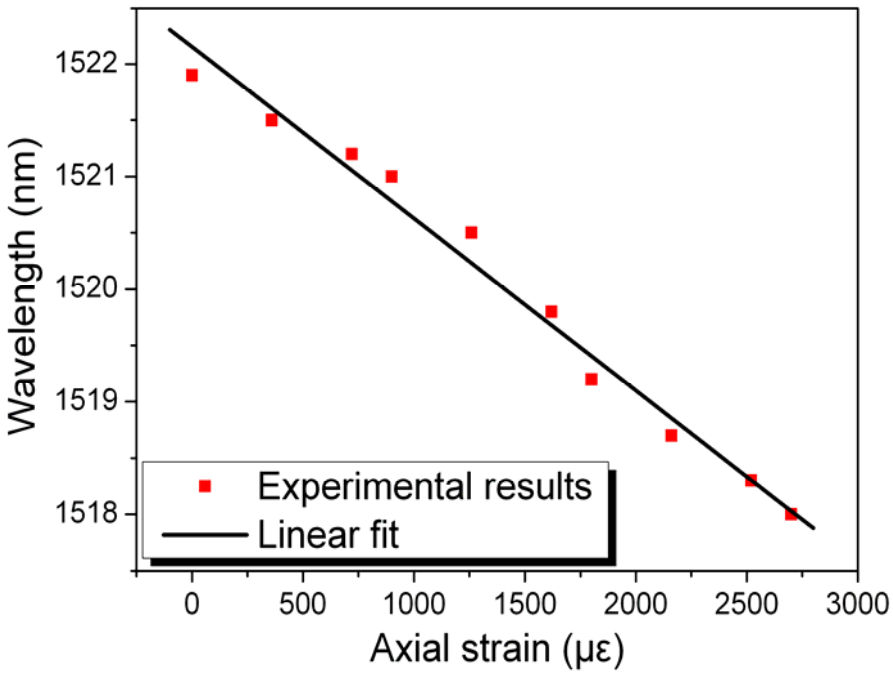

(b)

Fig.5.3.(a) The transmission spectra of the device at different strains.(b) Fringe dip wavelength shift with applied axial strain.

5.4 Thermal Response

The dip wavelength shift with the temperature variation is demonstrated in Fig. 5.4(a). Fig 5.4(b) shows the transmission spectra of the same device sample used in the axial strain test, at different temperatures. A fringe dip near ~1523 nm at room temperature was found to experience a red shift with the increase of temperature. The temperature sensitivity obtained is ~9.8 pm/°C, close to that of FBG. Following the same analysis procedure used in deriving Eq. (4), the dip wavelength shift due to the temperature increase can be expressed as

$$\delta\lambda_{dip} = \frac{4}{2m+1}[n_{cl}\Delta x(\frac{x}{z}-\frac{n_{co}}{n_{cl}})+(z-x)\delta n_T] \approx \frac{4}{2m+1}(z-x)\delta n_T \tag{5.5}$$

where Δx is induced by material thermal-expansion and δn_T denotes the change in effective RI of silica, due to thermal-optical effect. The thermal-optical effect plays the dominant role in determining the dip wavelength shift as the thermo-optic coefficient (7.8×10^{-6}) is much larger than the thermal expansion coefficient (4.1×10^{-7}) in silica. Thus, when the temperature is increased, a red shift of dip wavelength appears, as indicated by Eq. (5).

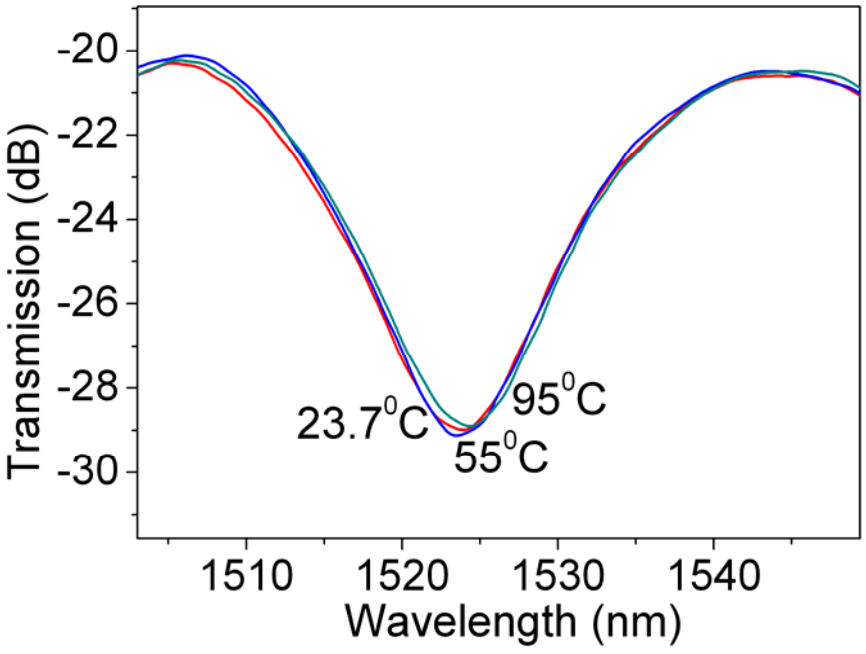

(a)

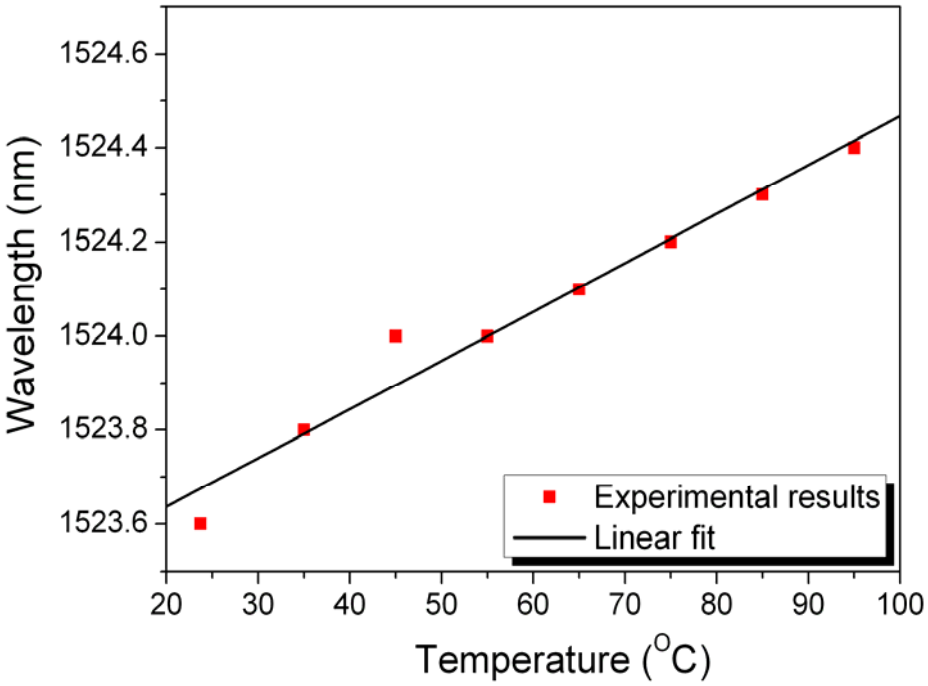

(b)

Fig. 5.4. (a) The transmission spectra of the device at different temperatures.
(b) Fringe dip wavelength shift with the temperature variation

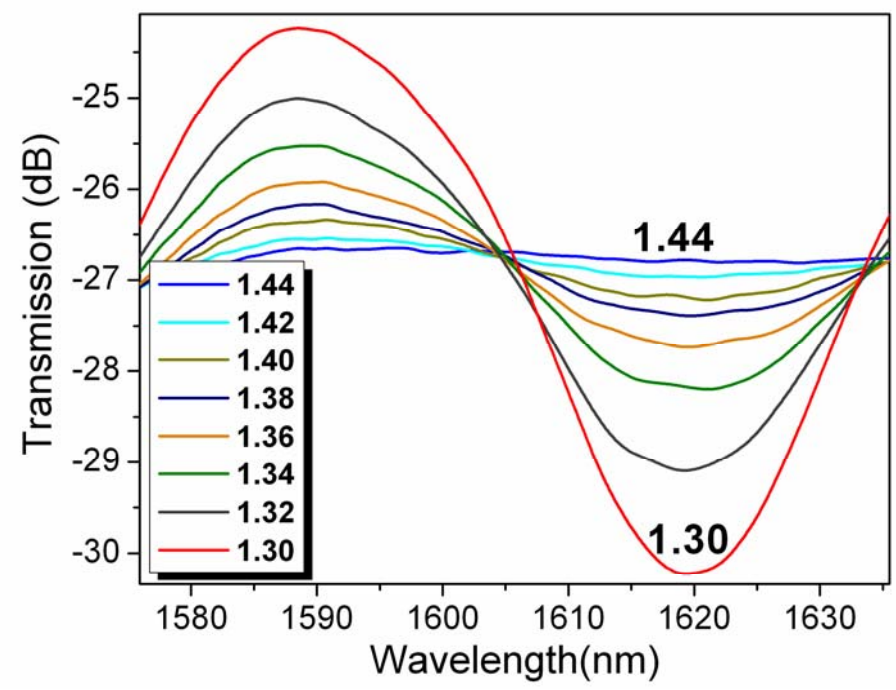

(a)

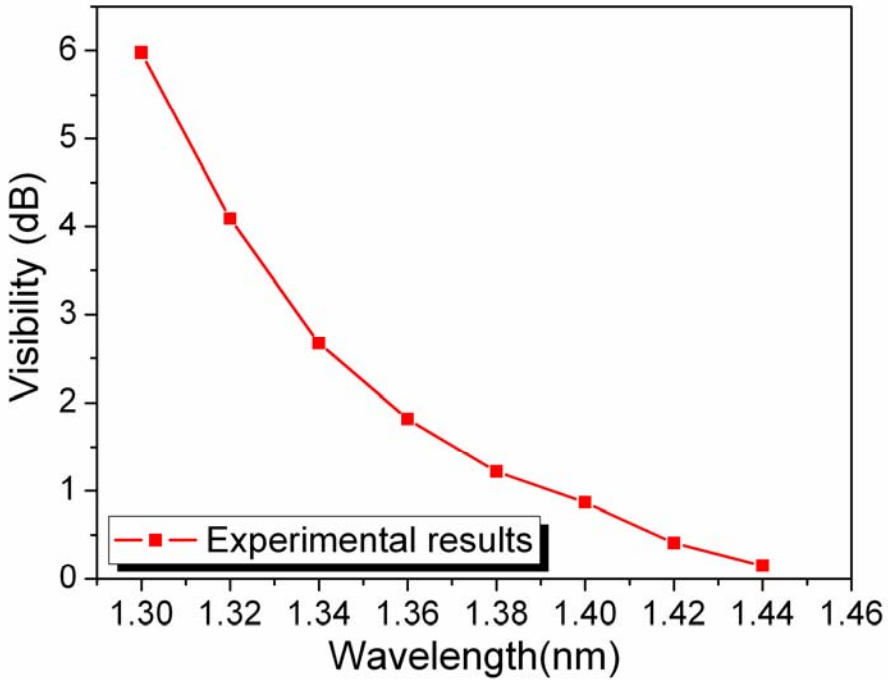

(b)

Fig. 5.5 (a) The transmission spectra of the device at different external RI values. (b) Variation of the output fringe visibility with external RI.

5.5 Refractive Index Response

The device sample with air spherical cavity separation of 265 μm was tested for RI sensing to verify its response to external environment. The device was immersed in a series of RI liquids (from Cargille Laboratories) in the RI range of 1.30-1.44 (at 489.3 nm) with an interval of 0.02. Each time after the measurement, the fiber device was rinsed with methanol carefully until the original spectrum (i.e., the reference spectrum) could be restored and no residue liquid was left on the fiber surface. The variation of the fringe visibility with the RI change is shown in Fig. 5.5, where the inset reveals the transmission spectra within the wavelengths range between 1575 and 1635 nm. It can be found from the figure that the visibility of the output fringe pattern critically depends on the RI and is gradually decreased when the RI value is increased from 1.33 and approaches to zero when the RI value reaches 1.44. This is due to the fact that when the RI value of the surrounding environment becomes nearly the same as that of the fiber cladding, the light beam would directly come out from the optical fiber and enter into the surrounding medium without reflection. The highest sensitivity obtained is ~75.6 dB/RIU at the RI value of 1.30.

5.6 Curvature Response

The device sample with air spherical cavity separation of 265 μm was also tested in the bending measurement. The sample was closely attached on the central part of a flexible steel ruler fixed between two translation stages, which was moved inward to induce a bend in the ruler and, hence, in the fiber device. The sensor curvature is given by [3], where l is the distance between the edges of the two stages, and d is the bending displacement at the center of the fiber in-line MZI. As shown in Fig. 5.6 and its inset, the fringe dip wavelength close to 1485 nm does not shift with

curvature. This can be explained by the fact that there is essentially no change in the optical path lengths of the two interferometer arms when the curvature is varied and hence no OPD change is generated.

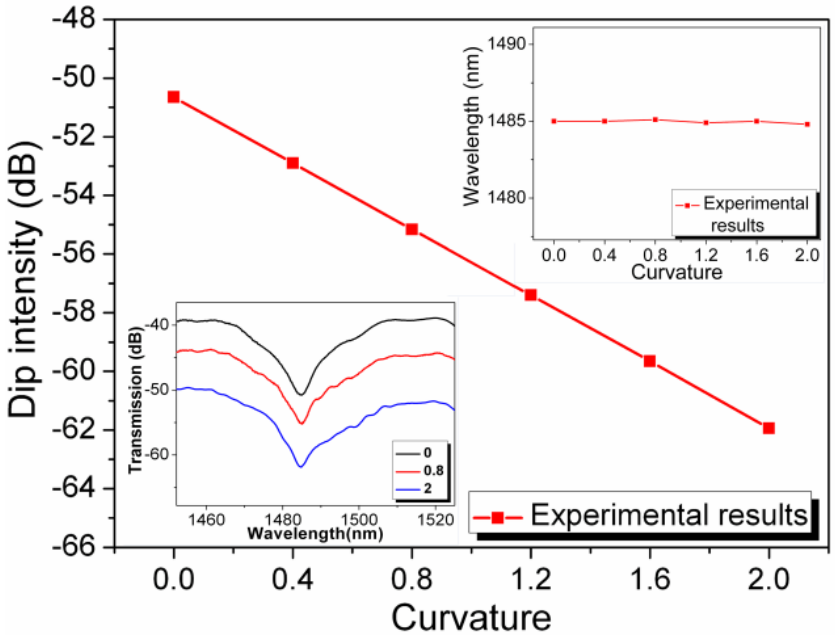

Fig. 5.6 Dip intensity versus the curvature. Upper inset shows fringe dip wavelength versus curvature; and the lower shows the transmission spectra of the device at curvature ratios of 0, 0.8 and 2 m^{-1}, respectively.

5.7 Polarization Analysis

Visibility of the asymmetrical optical device is influenced by the polarization from the two beams because the values of corresponding Brewster angle for O light and E light are different. Different portion of O and E light may lead to different reflectivity on the inner mirrors, which contributes to different intensity splitting ratio and influence the visibility. To test the polarization influence on our device, we did an experiment to test the polarization effect on visibility. We observe the

visibility with different polarization by using a polarization controller. The Fig. 5.7 shown below consists of the largest and the least visibility. The influence from polarization exists but is very little. The maximum visibility is 13.51 dB and the minimum visibility is 13.01 dB. Both visibilities are suitable for observation.

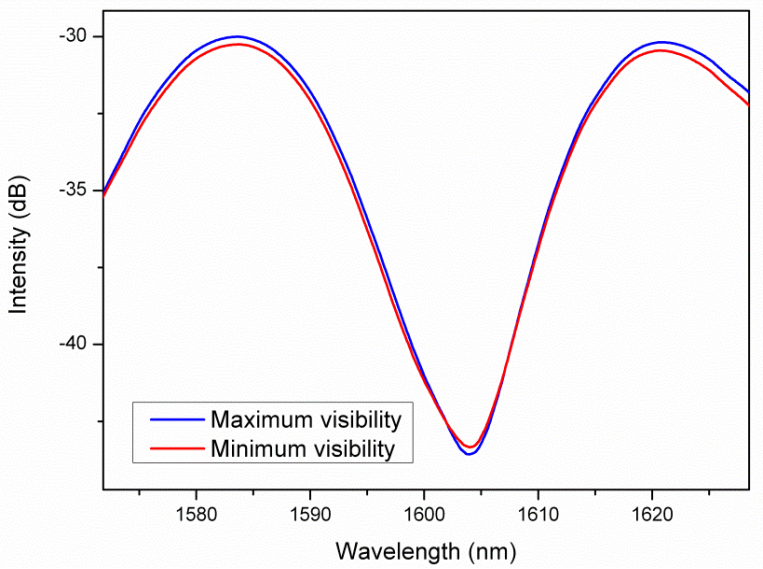

Fig. 5.7. Dip intensity at different polarization position. Red and blue curve shows the maximum visibility and minimum visibility at different polarization.

5.8 Summary and Discussion

In conclusion, the surfaces of the air spherical cavity pair positioned adjacent to the fiber core play the role of fiber internal mirrors, which effectively reflect part of the incident light beam in the fiber core to the air–cladding interface, where, after experiencing another reflection, the light beam returns to the fiber core, and recombines with the light beam remaining in the fiber core to form a fiber in-line MZI.

It is interesting to notice that in our device, the change in surrounding RI leads to a

change in output fringe visibility, the variation in temperature only shifts the fringe dip wavelength, and the change in curvature merely causes a change in fringe dip intensity; i.e., three parameter sensing can be simultaneously achieved, and thus the temperature cross sensitivity can be eliminated.

Such an inner structure-based fiber device is miniature, robust, suitable for high-accuracy measurement, sensitive to the surrounding environment, and free of temperature cross sensitivity, thus exhibiting high potential in versatile photonic applications.

Reference

[1] C. Chen, A. Laronche, G. Bouwmans, et al, “Sensitivity of photonic crystal fiber modes to temperature, strain and external refractive index,” Opt. Express 16, 9645-9653 (2008)

[2] N. Liu, Y. Li, Y. Wang, H. Wang, et al, “Bending insensitive sensors for strain and temperature measurements with Bragg gratings in Bragg fibers,” Opt. Express 19, 13880-13891 (2011)

[3] Y. P. Wang, Y. J. Rao, Z. L. Ran, et al, “Bend-insensitive long-period fiber grating sensors,” Opt. Lasers Eng. 41, 233-239 (2004)

Chapter 6

Conclusion and Further Work

6.1 Conclusion

In this thesis, we have investigated the fiber sensors based on inner air cavity, and four different sensors have been proposed. The content of this dissertation is addressed as:

We designed and fabricated a series of inner air cavities with different morphology by use of parameter controlling of fs laser micromachining system and fusion splicing program. An inner air cavity could be fabricated by drilling a micro-hole on cleaved fiber tip and then fusing such a fiber tip with another cleaved fiber tip. The morphology of the inner air cavity could be controlled by adjusting: (1) The size and position of the micro-hole (2) Fusion current and (3) Fusion time.

One intrinsic fiber in-line FPI sensor for refractive index is proposed in this thesis. For sensing surrounding RI, a vertical micro channel is drilled by fs laser through the air cavity, enabling the surrounding liquid to flow in and out. The RI sensitivity achieved in the experiment is ~994 nm/RIU, and the temperature cross-sensitivity is as low as~4.8×10^{-6} RIU/°C.

A MZI sensor for high temperature based on an air cavity with micro-structure adjacent to fiber core is fabricated by fs laser with fusion splicing technology. When the light beam in the core reaches the air cavity, part of the light beam is coupled into the air cavity as leaky mode and the other part of the light beam remains in the core.

These two beams recombine in the fiber core at the end of the air cavity. This MZI exhibits temperature sensitivity of 43.2 nm/^{o}C up to 1000 ^{o}C and is free of cross sensitivity to RI.

For hydrogen sensing, another fiber in-line sensor is proposed based on air cavity with micro-structure. After inscribing a periodical microstructure on the air cavity's surface adjacent to fiber core and coating Pt-doped WO_3 on the fiber surface, a hydrogen fiber sensor is fabricated. The Pt-doped WO_3 coated fiber device exhibits wavelength shift of 2.64 nm when hydrogen concentration is increased from 0 to 4%.

A MZI based on dual internal mirrors formed by an air cavity pair adjacent to fiber core is fabricated by fs laser with fusion splicing technology. The smooth surface of the air cavity could serve as inner mirror, reflecting part of the incident light beam to the air-cladding to form a new optical path other than the fiber core. A large optical length difference and small FSR could be observed. This device could simultaneously sense three parameters including RI, temperature and curvature.

Compared with conventional fiber sensors, the fiber sensors based on inner air cavity proposed in this thesis own the features as following:

(1) Robust in mechanical strength. The fiber with inner air cavity fabricated by use of fs laser micromachining and fusion splicing technique is not tapered nor damaged, exhibiting great robustness. What's more, the fusion program used in our experiments with the large fusion current and long fusion time makes the fiber joints sound and firm. In chapter 3, we tested the device's tolerance range of axial strain. The wide strain measurement range achieved is up to 3157 με, which indicates the robustness of this structure.

(2) Compact in size. All these four fiber sensors are compact in size. The lengths of the fiber sensors based on solo cavity in chapter 2, chapter 3 and chapter 4 are below 50 μm; and the length the fiber sensor based on dual cavities in chapter 5 is below 200 μm. To reduce the size of MZI, we designed two structures: (1) Core-air-mode MZI in chapter 3. (2) MZI based on inner mirrors in chapter 5. These two structures provide approaches to fabricate ultra-compact MZIs.

(3) A variety of microstructures are designed. Compared with the fiber sensors introduce in chapter 1, which are merely based on the air cavity, the sensors in this thesis are with some well-designed microstructures. In chapter 2, two micro channels are fabricated to cross the cavity to allow the surrounding liquid to flow in and out. In chapter 3, a microstructure is fabricated to remove the smooth surface of the cavity and eliminate the unwanted interference. In chapter 4, a periodic microstructure introduces a structure modulation on the fiber core, and converts part of the incident light beam into cladding mode. These microstructures provide the fiber sensors based on air cavity high potential in versatile photonic applications.

(4) Great sensing performance. The fiber sensors in chapter 2, chapter 3 and chapter 4 exhibit high sensitivity and low cross sensitivity. The fiber sensor in chapter 5 is capable of performing simultaneous sensing for temperature, RI and curvature without crosstalk. The great sensing performance makes these fiber sensors valuable in industries like biology, chemistry, construction, mining and electrical engineering.

6.2 Further Work

Fiber inner air cavity and other microstructures fabricated by fs laser micromachining technique are promising in optical sensing applications. Based on these microstructures, some other optical fiber devices could be designed and fabricated in the future. The future work can be suggested as follows:

(1) If an air spherical cavity adjacent to fiber core is infiltrated with RI slightly larger than fiber core, the infiltrated cavity could sever as a resonator cavity. The light beam in the fiber might be coupled into the infiltrated cavity and excite a whispering-gallery-mode (WGM) around the cavity. Based on this theory, an ultra-compact fiber in-line WGM resonator could be developed, with potential application in all optical system for sensing, filtering, and frequency stabilization.

(2) We could design a device based inner mirror to excite surface plasmon. When the optical device in Chapter 5 is coated with a metal such as Au, the light beam transmitting through the fiber core would be reflected by the inner mirror to coating-cladding interface, and after that the light beam would be reflected back to fiber core. When the width of coating and the reflection angle is precisely controlled during the fabrication process, the light would interact with the metal strongly and surface plasmon could be generated.

A surface grating for a beam splitter or beam shape controller is expected to be fabricated by fs laser micromachining technique. We have already achieved some progress in this project. We designed a micro periodic grating structure on the tip end of an optical fiber, which is covering the core of the

fiber.

The fs laser pulses (λ=800 nm) of 120 fs at a repetition rate of 1 kHz were focused onto the fiber by a 40× objective lens with an NA value of 0.66 and a working distance of 1.7 mm. A CCD camera was employed to monitor the fabrication process. A standard SMF-28 with effective RI of 1.4682 (at 1550 nm) was mounted on a computer controlled three-dimensional translation stage with 40 nm resolution. Each dot structure with a side length of ~1 μm and a depth of ~0.8 μm, was inscribed by fs laser pulses with energy of ~0.5 μJ for 1 second. We fabricated an inscribed two-dimensional diffraction grating structure with a 3 μm pitch as shown in Fig. 6.1(a). Obvious diffraction pattern of light existing the fiber tip end with 680 nm light source could be observed in Fig. 6.2(b).

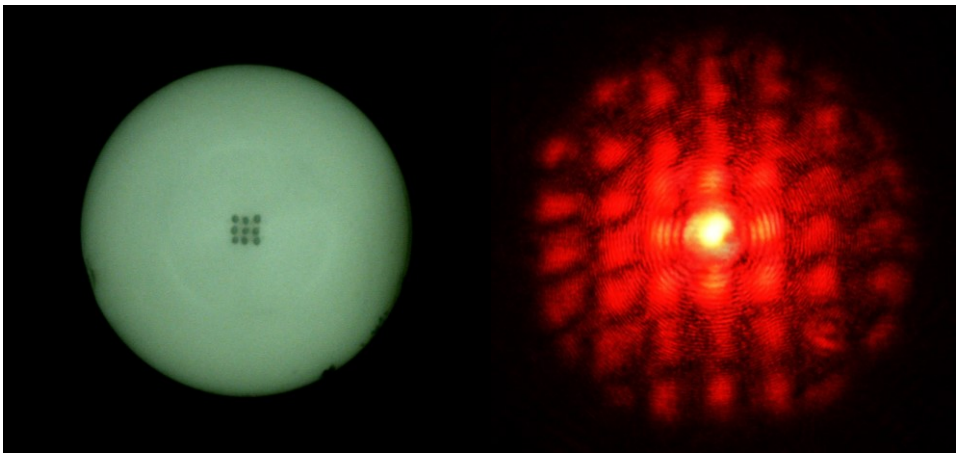

(a) **(b)**

Fig. 6.1(a) An inscribed two-dimensional diffraction grating structure with a 3 μm pitch. (b) Diffraction pattern of light existing the fiber tip end with 680 nm light source.

In order to enhanced grating efficiency of the certain order diffraction, the fabrication conditions need to be optimized in future work by adjusting the grating pitch and groove depth on the cleaved fiber tip. Analysis of diffraction beam patterns with white light source is about to be held in future, which is important for its potential application in wavelength-division multiplexing system [1]. Some other complex structures based on this fiber end tip grating will be fabricated for designing a beam splitter or beam shape controller in the next step.

Appendix

No.	Lens	Energy	Shape	Distance away from centre	Actual micro-hole size	Largest Depth	Fusion current	Fusion time	Cavity size
1	20×	2μJ	Square	0	1μm*1μm	1μm	16.3mA	2s	60μm
2	20×	2μJ	Square	0	1μm*1μm	1μm	15.3mA	1.5s	30μm
3	20×	2μJ	Square	0	1μm*1μm	1μm	16.8mA	2s	65μm
4	20×	2μJ	Square	0	12μm*12μm	17μm	17.3mA	2s	93μm
5	20×	3μJ	Square	15μm	Diameter: 20μm	23μm	14.3mA	1.5s	35μm
6	40×	1.5μJ	Circle	18μm	Diameter: 28μm	30μm	15.2mA	2s	79μm
7	40×	3μJ	Circle	20μm	Diameter: 22μm	35μm	14.3mA	1.5s	48μm

Tablet 6.1. Fabrication parameters used in thesis.

Reference

[1] W. Shin, I. B. Sohn, B.-A. Yu, et al, “Microstructured Fiber End Surface Grating for Coarse WDM Signal Monitoring,” IEEE Photo. Tech. Lett. 19(8) (2007)